Impact of 3-D Structures and Their Radiation on Thermal Infrared Measurements in Urban Areas

Xiaopo Zheng, Maofang Gao, Zhao-Liang Li, Kun-Shan Chen, Xia Zhang, Guofei Shang

Impact of 3-D Structures and Their Radiation on Thermal Infrared Measurements in Urban Areas

Xiaopo Zheng, Maofang Gao, Zhao-Liang Li, Kun-Shan Chen, *Fellow, IEEE*, Xia Zhang, and Guofei Shang

***Abstract*— Land surface temperature (LST) is a key parameter for many fields of study. Currently, LST retrieved from satellite thermal infrared (TIR) measurements is attainable with an accuracy of about 1 K for most natural flat surfaces. However, over urban areas, TIR measurements are influenced by 3-D structures and their radiation that could degrade the performance of existing LST retrieval algorithms. Therefore, quantitative models are needed to investigate such impact. Current 3-D radiative transfer models are generally based on time-consuming numerical integrations whose solutions are not analytical, and are therefore difficult to exploit in the methods of physical retrieval of LST in urban areas. This article proposes an analytical TIR radiative transfer model over urban (ATIMOU) areas that considers the impact of 3-D structures and their radiation. The magnitude of this impact on TIR measurements is investigated in detail, using ATIMOU, under various conditions. Simulations show that failure to acknowledge this impact can potentially introduce a 1.87-K bias to the ground brightness temperature for street canyon whose ratio "wall height/road width" is 2, wall and road temperature is 300 K, wall emissivity is 0.906, and road emissivity is 0.950. This bias reaches 4.60 K if road emissivity decreases to 0.921, and road temperature decreases to 260 K. ATIMOU is also compared to the discrete anisotropic radiative transfer (DART) model. Small mean absolute error of 0.10 K was found between the models regarding the simulated ground brightness temperatures, indicating that ATIMOU is in good agreement with DART.**

***Index Terms*— 3-D, land surface temperature (LST), radiative transfer, thermal infrared (TIR), urban areas.**

I. Introduction

LAND surface temperature (LST) is one of the most important Earth surface parameters, as it is the key factor affecting the energy balance of the Earth and is required by studies of global warming, evaporation, and urban heat islands [1]–[5]. Thermal infrared (TIR) remote sensing provides a suitable and efficient way to obtain accurate LST information from the Earth's surface. Regional and global LST may be obtained, based on TIR measurements, using existing LST retrieval algorithms. After decades of improvement, various types of LST retrieval algorithms have been developed [5]–[8] and have achieved great success for natural flat surfaces [9]–[15]. However, in urban areas, 3-D structures and their radiation affect satellite TIR measurements, especially in high spatial resolution images [16], [17], because the observed radiance would increase due to the radiation of the surroundings and reflections inside 3-D structures; the observed signal would be anisotropic through various viewing angles. Consequently, the performance of existing LST retrieval algorithms may deteriorate significantly if this impact is not well addressed in observed signals. Therefore, quantitative models are needed to investigate the impact of 3-D structures and their radiation on TIR measurements in urban areas.

To understand the anisotropic thermal behavior of urban areas, a number of previous researches have studied the 3-D surface modeling. Johnson *et al*. [18] proposed the surface heat island model (SHIM) to address the effects of building 3-D geometries. Voogt [19] developed a model to estimate the observed radiance in urban areas by considering five components: roof, sunlit and shadowed ground, sunlit and shadowed walls. Later, Krayenhoff and Voogt [20] proposed a more detailed model—temperatures of urban facets in 3-D (TUF-3D)—to study urban surface temperatures for a variety of surface geometries and properties. In their model, buildings were divided into cubic cells and internal building temperature was also considered. These three models are excellent thermal tools with which to estimate energy balance and study urban climate [21]; however, they do not allow for analysis of the dominating factors that impact satellite-observed TIR signals at the sensor level in detail [16]. Gastellu-Etchegorry *et al*. [22], [23] and Guillevic and Gastellu-Etchegorry [24] extended the discrete anisotropic radiative transfer (DART) model to the TIR region, providing a modified model capable of simulating the sensor-observed TIR spectral radiance of 3-D scenes. Although the current version of DART

Manuscript received December 2, 2019; revised March 16, 2020; accepted April 10, 2020. This work was supported by the China Scholarship Council (CSC). *(Corresponding authors: Zhao-Liang Li; Guofei Shang.)*

Xiaopo Zheng is with ICube (UMR 7357), CNRS, UdS, F-67412 Illkirch, France (e-mail: xiaopocpu@gmail.com).

Maofang Gao is with the Institute of Agricultural Resources and Regional Planning, Chinese Academy of Agricultural Sciences, Beijing 100081, China (e-mail: gaomaofang@caas.cn).

Zhao-Liang Li is with the Institute of Agricultural Resources and Regional Planning, Chinese Academy of Agricultural Sciences, Beijing 100081, China, and also with ICube (UMR 7357), CNRS, UdS, F-67412 Illkirch, France (e-mail: lizhaoliang@caas.cn).

Kun-Shan Chen is with the Henan International Joint Laboratory of Polarized Sensing and Intelligent Signal Processing, Xuchang University, Xuchang 461000, China (e-mail: chenks@radi.ac.cn).

Xia Zhang and Guofei Shang are with the College of Land Resources and Urban and Rural Planning, Hebei GEO University, Shijiazhuang 050031, China (e-mail: zhangx396@nenu.edu.cn; shangguofei@hgu.edu.cn).

Color versions of one or more of the figures in this article are available online at http://ieeexplore.ieee.org.

Digital Object Identifier 10.1109/TGRS.2020.2987880

can also allow a term by term analysis of the radiative contributors on the signal at a sensor level, the model should be run several times which is not convenient for schematic case studies [16], [17]. Thus, Pallotta *et al.* [17] developed another model to estimate the sensor-observed radiance. However, vertical surfaces such as building walls could only be processed approximately because this model used a regular grid to digitalize the relief. Fontanilles *et al.* [16] proposed the TIR radiance simulation with aggregation model (TITAN), which is able to study the main radiative sources in the urban areas observed by satellite. However, these three models all rely on discrete 3-D scenes of the Earth's surface and outputs were calculated based on time-consuming numerical integrations [16]. Additionally, as no analytical solutions have been provided for these models due to the complex calculation process involved, it is difficult to develop physical LST retrieval models for urban areas directly based on them. To our knowledge, the currently available analytical model for 3-D surface modeling is the one proposed by Caselles and Sobrino [25], which was designed for orange groves but could be applied to urban areas assuming the emissivity of roof is the same as the building walls. However, this model was derived on the basis of the linearization of Planck function using the first-order Taylor expansion, which maybe not accurate when the temperatures of each component inside the street canyon are not close to the overall effective brightness temperature. Besides, all the multireflections have been ignored in their model leading to the increase of bias as emissivity decreases. Therefore, to study the relationships between parameters of street canyons and their corresponding TIR measurements, a more accurate analytical TIR radiative transfer model with consideration of the impact of 3-D structures and their radiation is required.

This article proposes a new model, the analytical TIR radiative transfer model over urban (ATIMOU) areas, which could provide analytical solutions of the ground and satellite TIR measurement in urban areas. Application of this model to different street canyon scenarios allows for a detailed quantitative investigation of the impact of 3-D structures and their radiation on the TIR measurements. The ATIMOU is also compared to other existing models including the DART. This article is organized as follows: Section II describes the mathematical formulations of the proposed model. Section III analyzes the magnitude of the impact of 3-D structures and their radiation on TIR measurement under different conditions. Section IV provides the results of comparison between the proposed ATIMOU and other models. Finally, Section V summarizes the main findings.

II. Methodology

In this article, a street canyon in an urban area is defined as two buildings situated on either side of a road and oriented in a north–south direction. The 3-D structure is illustrated in Fig. 1 with W, L, and H representing the road width, road length, and wall height, respectively. Atmospheric spherical albedo at the bottom of the atmosphere is represented by ρ_A, and $L^{\downarrow}$ is the atmospheric downwelling radiance (wavelength λ is omitted here and hereafter for simplicity). The cross-section of the atmosphere above the road at the roof level, i.e., the plane $A_1A_2A_3A_4$ in Fig. 1, is denoted A. The emissivity of the roof, left wall (LW), road (Rd), and right wall (RW) are symbolized as $\varepsilon_{\text{roof}}$, ε_{LW}, ε_{Rd}, and ε_{RW}, respectively, while LST_{roof}, LST_{LW}, LST_{Rd}, and LST_{RW} are the corresponding temperatures. Moreover, two additional assumptions have been made for simplicity: 1) the walls of the building are all perpendicular to the ground and have the same height and 2) all facets are Lambertian and flat. Using the parameters of the scenario described above, the ATIMOU is developed in the following sections.

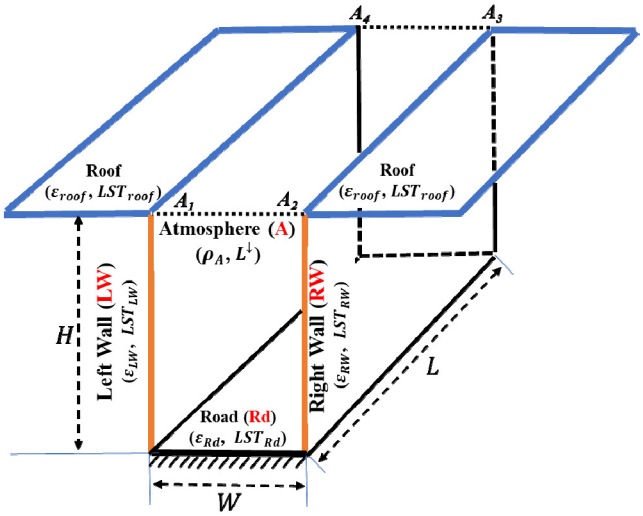

Fig. 1. Illustration of a street canyon in an urban area. W, L, and H are the road width, road length, and wall height, respectively. ρ_A is the atmospheric spherical albedo at the bottom of the atmosphere and $L^{\downarrow}$ is the atmospheric downwelling radiance. $\varepsilon_{\text{roof}}$, ε_{LW}, ε_{Rd}, and ε_{RW} are the emissivity of roof, left wall, road, and right wall respectively, whereas LST_{roof}, LST_{LW}, LST_{Rd}, and LST_{RW} are the corresponding temperatures.

A. Development of the Analytical Model for Radiative Transfer Over a Street Canyon

When considering 3-D structures in urban areas, the compositions inside the instantaneous field of view (IFOV) may vary with viewing angle and IFOV size. Consequently, the impact of 3-D structures and their radiation on ground observed radiance of the target pixel could be different for different conditions.

To determine the ground observed radiance of the target pixel, the 3-D structure of an urban area was first projected onto the ground along the direction of view. Then the solid angles of the projections of each composition inside the IFOV of the sensor were calculated (Fig. 2), allowing the proportion of each composition in the target pixel to be determined. Finally, the ground observed radiance of the target pixel could be estimated using the weighted sum method (1). However, the radiance of each composition used in the weighted sum method should not be their self-emitted radiance; rather, it should be their surface-leaving radiance considering the impact of 3-D structures and their radiation. Since building roofs are not affected by 3-D structures and their radiation in

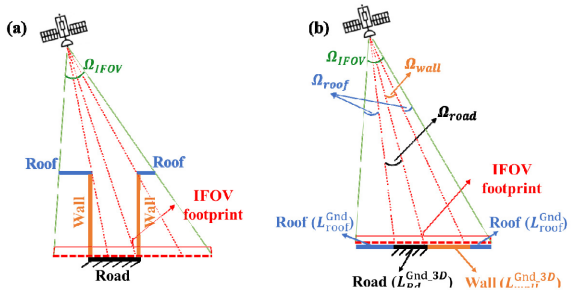

Fig. 2. Illustrations of (a) viewing geometry of the 3-D structures in urban areas and (b) 2-D projection of 3-D structures in urban areas. The solid angle of the entire IFOV of the sensor is represented by Ω_{IFOV}, whereas Ω_{roof}, Ω_{road}, and Ω_{wall} are the solid angles of the projections regarding to the components of roof, road, and wall inside the IFOV of the sensor, respectively.

urban areas, the corresponding ground observed radiance of a roof can be calculated using (2), according to the traditional radiative transfer model [15], [26], [27]

$$L^{\mathrm{Gnd\_3D}} = B\left(T^{\mathrm{Gnd\_3D}}\right) = \frac{\Omega_{\mathrm{roof}}}{\Omega_{\mathrm{IFOV}}} L^{\mathrm{Gnd}}_{\mathrm{roof}} + \frac{\Omega_{\mathrm{road}}}{\Omega_{\mathrm{IFOV}}} L^{\mathrm{Gnd\_3D}}_{\mathrm{Rd}} + \frac{\Omega_{\mathrm{wall}}}{\Omega_{\mathrm{IFOV}}} L^{\mathrm{Gnd\_3D}}_{\mathrm{wall}} \quad (1)$$

in which

$$L^{\mathrm{Gnd}}_{\mathrm{roof}} = \varepsilon_{\mathrm{roof}} B(\mathrm{LST}_{\mathrm{roof}}) + (1-\varepsilon_{\mathrm{roof}}) L^{\downarrow} \quad (2)$$

where $L^{\mathrm{Gnd\_3D}}$ and $T^{\mathrm{Gnd\_3D}}$ are, respectively, the ground observed radiance and brightness temperature of the target pixel with impact of 3-D structures and their radiation; $B(T)$ is the Planck function at temperature T; Ω_{IFOV} is the solid angle of the entire IFOV of the sensor; Ω_{roof}, Ω_{road}, and Ω_{wall} are the solid angles of the projections regarding to the components of roof, road, and wall inside the IFOV of the sensor, respectively, which are not only dependent on the viewing zenith and azimuth angles, but also dependent on the geometric parameters of the street canyon. Besides, the parallel projection method has been used in this article to determine the projected area of each component inside the sensor's IFOV along the viewing direction; $L^{\mathrm{Gnd}}_{\mathrm{roof}}$ is the ground observed radiance of the roof and will not be affected by the 3-D structures and their radiation; and $L^{\mathrm{Gnd\_3D}}_{\mathrm{Rd}}$ and $L^{\mathrm{Gnd\_3D}}_{\mathrm{wall}}$ are, respectively, the ground observed radiance of the road and wall with the impact of 3-D structures and their radiation. Moreover, because the parallel projection method has been used as stated above, only one building wall could be observed by the remote sensor given a specific viewing direction. Therefore, assuming $L^{\mathrm{Gnd\_3D}}_{\mathrm{LW}}$ and $L^{\mathrm{Gnd\_3D}}_{\mathrm{RW}}$ are the ground observed radiance of the left wall and right wall with the impact of 3-D structures and their radiation, respectively, $L^{\mathrm{Gnd\_3D}}_{\mathrm{wall}}$ is then equal to $L^{\mathrm{Gnd\_3D}}_{\mathrm{LW}}$ or $L^{\mathrm{Gnd\_3D}}_{\mathrm{RW}}$ depending on the viewing angle. As a result, $L^{\mathrm{Gnd\_3D}}_{\mathrm{Rd}}$, $L^{\mathrm{Gnd\_3D}}_{\mathrm{LW}}$, and $L^{\mathrm{Gnd\_3D}}_{\mathrm{RW}}$ are the critical parameters for developing the analytical model.

When the 3-D structures in urban areas are taken into consideration, the environmental radiance above the road and wall is no longer determined solely by atmospheric downwelling radiance, but also by the radiation of surroundings and the reflections inside the 3-D structures. Inside the street canyon, energy is mainly exchanged among four components: the atmosphere, left wall, road, and right wall (Fig. 1). As stated above, the ground observed radiance of the road is $L^{\mathrm{Gnd\_3D}}_{\mathrm{Rd}}$, then the power that leaves the surface of the road (Q_{Rd}) can be expressed by the following equation:

$$Q_{\mathrm{Rd}} = L \cdot W \cdot \pi L^{\mathrm{Gnd\_3D}}_{\mathrm{Rd}}. \quad (3)$$

In addition, considering that the emissivity and temperature of the road are $\varepsilon_{\mathrm{Rd}}$ and $\mathrm{LST}_{\mathrm{Rd}}$, respectively, the power that comes from the surroundings and arrives at the road is $Q^{\mathrm{Evn\_3D}}_{\mathrm{Rd}}$, then the power that leaves the surface of the road (Q_{Rd}) can also be expressed by

$$Q_{\mathrm{Rd}} = L \cdot W \cdot \pi \varepsilon_{\mathrm{Rd}} B(\mathrm{LST}_{\mathrm{Rd}}) + (1-\varepsilon_{\mathrm{Rd}}) Q^{\mathrm{Evn\_3D}}_{\mathrm{Rd}}. \quad (4)$$

Combining (3) and (4), (5) could be obtained

$$L \cdot W \cdot \pi L^{\mathrm{Gnd\_3D}}_{\mathrm{Rd}} = L \cdot W \cdot \pi \varepsilon_{\mathrm{Rd}} B(\mathrm{LST}_{\mathrm{Rd}}) + (1-\varepsilon_{\mathrm{Rd}}) Q^{\mathrm{Evn\_3D}}_{\mathrm{Rd}} \quad (5)$$

in which

$$Q^{\mathrm{Evn\_3D}}_{\mathrm{Rd}} = L \cdot W \cdot \pi L^{\mathrm{Gnd\_3D}}_{A} \cdot F_{A\to\mathrm{Rd}} + L \cdot H \cdot \pi L^{\mathrm{Gnd\_3D}}_{\mathrm{LW}} \cdot F_{\mathrm{LW}\to\mathrm{Rd}} + L \cdot H \cdot \pi L^{\mathrm{Gnd\_3D}}_{\mathrm{RW}} \cdot F_{\mathrm{RW}\to\mathrm{Rd}} \quad (6)$$

where $L^{\mathrm{Gnd\_3D}}_{A}$ is the radiance of the atmosphere with the impact of 3-D structures and their radiation, and $F_{\mathrm{X}\to\mathrm{Rd}}$ is the view factor from surface X to surface Rd ($\mathrm{X} = A, \mathrm{LW}, \mathrm{RW}$), which represents the fraction of energy leaving surface X that reaches surface Rd.

Substituting (6) into (5), the following equation can be obtained:

$$-W \cdot L^{\mathrm{Gnd\_3D}}_{\mathrm{Rd}} + (1-\varepsilon_{\mathrm{Rd}}) \left(W \cdot F_{A\to\mathrm{Rd}} \cdot L^{\mathrm{Gnd\_3D}}_{A} + H \cdot F_{\mathrm{LW}\to\mathrm{Rd}} \cdot L^{\mathrm{Gnd\_3D}}_{\mathrm{LW}} + H \cdot F_{\mathrm{RW}\to\mathrm{Rd}} \cdot L^{\mathrm{Gnd\_3D}}_{\mathrm{RW}}\right) + W \cdot \varepsilon_{\mathrm{Rd}} B(\mathrm{LST}_{\mathrm{Rd}}) = 0. \quad (7)$$

Similarly, three equations can be obtained for the surfaces of atmosphere (A), LW, and RW as follows:

$$-W \cdot L^{\mathrm{Gnd\_3D}}_{A} + \rho_A \left(H \cdot L^{\mathrm{Gnd\_3D}}_{\mathrm{LW}} \cdot F_{\mathrm{LW}\to A} + W \cdot L^{\mathrm{Gnd\_3D}}_{\mathrm{Rd}} \cdot F_{\mathrm{Rd}\to A} + H \cdot L^{\mathrm{Gnd\_3D}}_{\mathrm{RW}} \cdot F_{\mathrm{RW}\to A}\right) + W \cdot L^{\downarrow} = 0 \quad (8)$$

$$-H \cdot L^{\mathrm{Gnd\_3D}}_{LW} + (1-\varepsilon_{\mathrm{LW}}) \left(W \cdot L^{\mathrm{Gnd\_3D}}_{A} \cdot F_{A\to\mathrm{LW}} + W \cdot L^{\mathrm{Gnd\_3D}}_{\mathrm{Rd}} \cdot F_{\mathrm{Rd}\to LW} + H \cdot L^{\mathrm{Gnd\_3D}}_{\mathrm{RW}} \cdot F_{\mathrm{RW}\to LW}\right) + H \cdot \varepsilon_{LW} B(\mathrm{LST}_{\mathrm{LW}}) = 0 \quad (9)$$

$$-H \cdot L^{\mathrm{Gnd\_3D}}_{\mathrm{RW}} + (1-\varepsilon_{\mathrm{RW}}) \left(W \cdot L^{\mathrm{Gnd\_3D}}_{A} \cdot F_{A\to\mathrm{RW}} + H \cdot L^{\mathrm{Gnd\_3D}}_{\mathrm{LW}} \cdot F_{LW\to\mathrm{RW}} + W \cdot L^{\mathrm{Gnd\_3D}}_{\mathrm{Rd}} \cdot F_{\mathrm{Rd}\to\mathrm{RW}}\right) + H \cdot \varepsilon_{\mathrm{RW}} B(\mathrm{LST}_{\mathrm{RW}}) = 0 \quad (10)$$

where $F_{P\to Q}$ represents the view factor from surface P to surface Q (P, Q = Rd, A, LW, RW and $P \neq Q$). Combining (7)–(10), an equation system can be obtained with four unknowns, three of which are the required parameters $L^{\mathrm{Gnd\_3D}}_{\mathrm{Rd}}$, $L^{\mathrm{Gnd\_3D}}_{\mathrm{LW}}$, and $L^{\mathrm{Gnd\_3D}}_{\mathrm{RW}}$ in the following equations:

$$A\left[\, L^{\mathrm{Gnd\_3D}}_{\mathrm{Rd}} \quad L^{\mathrm{Gnd\_3D}}_{A} \quad L^{\mathrm{Gnd\_3D}}_{\mathrm{LW}} \quad L^{\mathrm{Gnd\_3D}}_{\mathrm{RW}} \,\right]^{T} = B \quad (11)$$

in which, (12) and (13), as shown at the bottom of this page.

After the matrix manipulation of $\boldsymbol{A^{-1}B}$, the four unknowns can be obtained and $L^{\text{Gnd\_3D}}$ can be expressed by an analytical equation after combining (1), (2), (11), (12), and (13), provided that the geometric and radiative properties of the street canyon are known. In addition, according to the traditional radiative transfer model, the satellite observed radiance ($L^{\text{TOA\_3D}}$) and brightness temperature ($T^{\text{TOA\_3D}}$) of the target pixel over a street canyon with impact of 3-D structures and their radiation could be expressed by

$$L^{\text{TOA\_3D}} = B(T^{\text{TOA\_3D}}) = \tau(\theta)L^{\text{Gnd\_3D}} + L^{\uparrow}(\theta) \quad (14)$$

where $\tau(\theta)$ and $L^{\uparrow}(\theta)$ are the total atmospheric transmittance and atmospheric upwelling radiance along the viewing direction with zenith angle of θ, respectively.

B. Simplification of the Analytical Model for Radiative Transfer Over a Street Canyon

In Section II-A, the exact solutions of $L_{\text{Rd}}^{\text{Gnd\_3D}}$, $L_{A}^{\text{Gnd\_3D}}$, $L_{\text{LW}}^{\text{Gnd\_3D}}$, and $L_{\text{RW}}^{\text{Gnd\_3D}}$ have been provided in the matrix form ($\boldsymbol{A^{-1}B}$), because their analytical forms are very complex. Therefore, they are very difficult to use to analyze the relationships between the input parameters and the magnitude of the impact of 3-D structures and their radiation. In this section, these analytical solutions have been simplified after applying some reasonable assumptions.

Considering that the two walls are parallel to each other, some of the view factors in (12) are therefore equivalent. Assuming that the length of the road and building is infinite, these view factors can be classified into two types: one is the view factor between "two infinitely long, directly opposed parallel plates of the same finite width" [28] represented by $F_{\text{Rd}\to A}$, $F_{A\to\text{Rd}}$, $F_{\text{RW}\to\text{LW}}$, $F_{\text{LW}\to\text{RW}}$; the other is the view factor between "two infinitely long plates of unequal widths, having one common edge, and at an angle of 90° to each other" [28] represented by $F_{A\to\text{LW}}$, $F_{\text{Rd}\to\text{LW}}$, $F_{A\to\text{RW}}$, $F_{\text{Rd}\to\text{RW}}$, $F_{\text{LW}\to A}$, $F_{\text{RW}\to A}$, $F_{\text{LW}\to\text{Rd}}$, and $F_{\text{RW}\to\text{Rd}}$. According to [28], the former can be calculated using (15) and (16) while the latter can be calculated using (17) and (18)

$$F_{\text{Rd}\rightleftharpoons A} = F_{\text{Rd}\to A} = F_{A\to\text{Rd}} = \sqrt{1+\left(\frac{H}{W}\right)^2} - \frac{H}{W} \quad (15)$$

$$F_{\text{RW}\rightleftharpoons\text{LW}} = F_{\text{RW}\to\text{LW}} = F_{\text{LW}\to\text{RW}} = \sqrt{1+\left(\frac{W}{H}\right)^2} - \frac{W}{H} \quad (16)$$

$$F_{A,\text{Rd}\to\text{LW,RW}} = F_{A\to\text{LW}} = F_{\text{Rd}\to\text{LW}} = F_{A\to\text{RW}} = F_{\text{Rd}\to\text{RW}} = 0.5\left[\frac{H}{W} + 1 - \sqrt{\left(\frac{H}{W}\right)^2 + 1}\right] \quad (17)$$

$$F_{\text{LW,RW}\to A,\text{Rd}} = F_{\text{LW}\to A} = F_{\text{RW}\to A} = F_{\text{LW}\to\text{Rd}} = F_{\text{RW}\to\text{Rd}} = 0.5\left[\frac{W}{H} + 1 - \sqrt{\left(\frac{W}{H}\right)^2 + 1}\right]. \quad (18)$$

After applying (15)–(18), the analytical solutions of $L_{\text{Rd}}^{\text{Gnd\_3D}}$, $L_{A}^{\text{Gnd\_3D}}$, $L_{\text{LW}}^{\text{Gnd\_3D}}$, and $L_{\text{RW}}^{\text{Gnd\_3D}}$ then can be expressed as follows (19), as shown at the bottom of the next page. in which, (20)–(28), as shown at the bottom of the next page.

Please note that these solutions contain all the energy exchanges inside the street canyon including the entire multiple reflections. However, they are still complex. Considering that the items regarding to the radiation that having been reflected more than once would add only a negligible contribution to the observed signals, it is reasonable to ignore them to simplify the analytical model.

In addition, if the emissivities of the left and right walls are assumed to be the same, i.e., $\varepsilon_{\text{LW}} = \varepsilon_{\text{RW}} = \varepsilon_{\text{wall}}$, then $L_{\text{Rd}}^{\text{Gnd\_3D}}$, $L_{A}^{\text{Gnd\_3D}}$, $L_{\text{LW}}^{\text{Gnd\_3D}}$, $L_{\text{RW}}^{\text{Gnd\_3D}}$ in (19) could be simplified further after complex mathematical derivation as follows (29), as shown at the bottom of the 6 page, where $\rho_{\text{wall}} = 1 - \varepsilon_{\text{wall}}$ represents the reflectance of the wall and $\rho_{\text{Rd}} = 1 - \varepsilon_{\text{Rd}}$ represents the reflectance of the road.

After simplification, each analytical solution in (29) consists of four parts with specific physical meanings. Taking $L_{\text{Rd}}^{\text{Gnd\_3D}}$ as an example, the term $\varepsilon_{\text{Rd}}B(\text{LST}_{\text{Rd}})$ on the right side of the equation represents the radiation from the road itself. The second term, $\rho_{\text{Rd}}H \cdot F_{\text{LW}\to\text{Rd}}\varepsilon_{\text{wall}}B(\text{LST}_{\text{LW}})/W(1 - F_{\text{RW}\rightleftharpoons\text{LW}}\rho_{\text{wall}})$, represents the radiation that is emitted by the left wall, then reaches the road surface, and is reflected by the road into the sensor. To be specific, two radiative transfer processes are included in this term: 1) the left wall-emitted radiation reaches the road surface directly, then is reflected by the road and 2) the left wall-emitted radiation is firstly reflected between the two walls for multiple times, then reaches the road surface, and is reflected by the road. The physical meanings of the third term $\rho_{\text{Rd}}H \cdot F_{\text{RW}\to\text{Rd}}\varepsilon_{\text{wall}}B(\text{LST}_{\text{RW}})/W(1 - F_{\text{RW}\rightleftharpoons\text{LW}}\rho_{\text{wall}})$ and the fourth term $\rho_{\text{Rd}}F_{A\to\text{Rd}}L^{\downarrow}/1 - F_{\text{RW}\rightleftharpoons\text{LW}}\rho_{\text{wall}}$ are similar to the second term but are regarding to the radiation emitted by the right wall and atmosphere, respectively. Besides, the remaining three analytical solutions ($L_{A}^{\text{Gnd\_3D}}$, $L_{\text{LW}}^{\text{Gnd\_3D}}$, and $L_{\text{RW}}^{\text{Gnd\_3D}}$) can also be interpreted similarly.

Provided that the road width, wall height, temperature and emissivity of the road and wall, atmospheric spherical albedo at the bottom of the atmosphere, and the atmospheric

$$A = \begin{bmatrix} -W & (1-\varepsilon_{\text{Rd}})W \cdot F_{A\to\text{Rd}} & (1-\varepsilon_{\text{Rd}})H \cdot F_{\text{LW}\to\text{Rd}} & (1-\varepsilon_{\text{Rd}})H \cdot F_{\text{RW}\to\text{Rd}} \\ \rho_A W \cdot F_{\text{Rd}\to A} & -W & \rho_A H \cdot F_{\text{LW}\to A} & \rho_A H \cdot F_{\text{RW}\to A} \\ (1-\varepsilon_{\text{LW}})W \cdot F_{\text{Rd}\to\text{LW}} & (1-\varepsilon_{\text{LW}})W \cdot F_{A\to\text{LW}} & -H & (1-\varepsilon_{\text{LW}})H \cdot F_{\text{RW}\to\text{LW}} \\ (1-\varepsilon_{\text{RW}})W \cdot F_{\text{Rd}\to\text{RW}} & (1-\varepsilon_{\text{RW}})W \cdot F_{A\to\text{RW}} & (1-\varepsilon_{\text{RW}})H \cdot F_{\text{LW}\to\text{RW}} & -H \end{bmatrix} \quad (12)$$

$$B = \begin{bmatrix} -W \cdot \varepsilon_{\text{Rd}}B(\text{LST}_{\text{Rd}}) & -W \cdot L^{\downarrow} & -H \cdot \varepsilon_{\text{LW}}B(\text{LST}_{\text{LW}}) & -H \cdot \varepsilon_{\text{RW}}B(\text{LST}_{\text{RW}}) \end{bmatrix}^T. \quad (13)$$

downwelling radiance are known in advance, the radiance of each component inside the street canyon with the impact of 3-D structures and their radiation can be obtained using (29) easily. Consequently, the ground observed radiance ($L^{\text{Gnd\_3D}}$) and brightness temperature ($T^{\text{Gnd\_3D}}$) of the target pixel over a street canyon affected by the 3-D structures and their radiation can be simplified in (30), whereas the satellite observed radiance ($L^{\text{TOA\_3D}}$) and brightness temperature ($T^{\text{TOA\_3D}}$) of the target pixel over a street canyon influenced by the 3-D structures and their radiation can also be simplified in (31)

$$L^{\text{Gnd\_3D}} = B(T^{\text{Gnd\_3D}}) = \mathbf{M}\cdot\mathbf{N} \tag{30}$$

$$L^{\text{TOA\_3D}} = B(T^{\text{TOA\_3D}}) = \tau(\theta)(\mathbf{M}\cdot\mathbf{N}) + L^{\uparrow}(\theta) \tag{31}$$

in which (32) and (33), as shown at the bottom of the next page.

The subscripts "wall_x" and "wall_y" in (33) identify the left wall or right wall, which are dependent on the viewing angles because only one building wall could be observed by the remote sensor given a specific viewing direction as stated in Section II-A. According to (29), the "wall_x" should be "LW" and "wall_y" should be "RW" if the left wall is inside the sensor's IFOV; while the "wall_x" should be "RW" and "wall_y" should be "LW" if the right wall is inside the sensor's IFOV.

Finally, the ATIMOU can be successfully developed on the basis of the solutions of $L_{\text{Rd}}^{\text{Gnd\_3D}}$, $L_{A}^{\text{Gnd\_3D}}$, $L_{\text{LW}}^{\text{Gnd\_3D}}$, and $L_{\text{RW}}^{\text{Gnd\_3D}}$. In fact, three options have been provided to calculate these four parameters. First, on the basis of (11), which is in matrix form, but provides the most accurate solutions and requires the least assumptions. Second, on the basis of (19), which is in analytical form and includes the entire multiple reflections. Third, on the basis of (29), which is simplified from (19) assuming that the two walls have same emissivity, and the items regarding to the radiation that having been reflected more than once are negligible. Considering that the third option gives the simplest solutions with acceptable accuracies for most cases, they have been used in the following sections to study the magnitude of the impact of 3-D structures and their radiation under different conditions. However, if more accurate results are required, particularly for situations in which facets have low emissivity inside a street canyon, more exact solutions given by (19) and (29) with entire multireflections should be used in ATIMOU. In addition, since the obstructions of solar irradiance inevitably exist in urban areas during the daytime of a cloudless day, the input LST_{LW}, LST_{RW}, and LST_{Rd} in ATIMOU then should be given as their effective temperature with consideration of the temperature difference in the sunlit and shadowed areas. In this way, the ATIMOU is applicable to both night-time and daytime conditions.

C. Qualification of the Impact of 3-D Structures and Their Radiation on TIR Measurements Over a Street Canyon

From the analysis above, the ground and satellite TIR measurements with consideration of the impact of 3-D structures and their radiation could be expressed by (30) and (31), respectively. If the 3-D structures are not considered, then ground and satellite TIR measurements irrespective of the impact of 3-D structures and their radiation could be expressed by (34) and (35), respectively, according to the traditional radiative transfer model

$$L^{\text{Gnd}} = B(T^{\text{Gnd}}) = \boldsymbol{M}\cdot\boldsymbol{V} \tag{34}$$

$$L^{\text{TOA}} = B(T^{\text{TOA}}) = \tau(\theta)(\boldsymbol{M}\cdot\boldsymbol{V}) + L^{\uparrow}(\theta) \tag{35}$$

$$\boldsymbol{V} = \begin{bmatrix} \varepsilon_{\text{roof}}B(\text{LST}_{\text{roof}}) + (1-\varepsilon_{\text{roof}})L^{\downarrow} \\ \varepsilon_{\text{Rd}}B(\text{LST}_{\text{Rd}}) + (1-\varepsilon_{\text{Rd}})L^{\downarrow} \\ \varepsilon_{\text{wall}}B\left(\text{LST}_{\text{wall\_}x}\right) + (1-\varepsilon_{\text{wall}})L^{\downarrow} \end{bmatrix} \tag{36}$$

$$\begin{bmatrix} L_{\text{Rd}}^{\text{Gnd\_3D}} \\ L_{A}^{\text{Gnd\_3D}} \\ L_{\text{LW}}^{\text{Gnd\_3D}} \\ L_{\text{RW}}^{\text{Gnd\_3D}} \end{bmatrix} = \begin{bmatrix} \dfrac{W\cdot(C_{11}-\rho_A C_1)\cdot\varepsilon_{\text{Rd}}B(\text{LST}_{\text{Rd}}) + W\cdot\rho_{\text{Rd}}C_{12}\cdot L^{\downarrow} + H\cdot\rho_{\text{Rd}}(\rho_A F_{\text{RdA}}+1)C_2}{W\cdot m\_\text{denom}} \\ \dfrac{W\cdot(C_{11}-\rho_{\text{Rd}}C_1)\cdot L^{\downarrow} + W\cdot\rho_A C_{12}\cdot\varepsilon_{\text{Rd}}B(\text{LST}_{\text{Rd}}) + H\cdot\rho_A(\rho_{\text{Rd}}F_{\text{RdA}}+1)C_2}{W\cdot m\_denom} \\ \dfrac{H\cdot(C_{31}-\rho_{\text{RW}}C_3)\cdot\varepsilon_{\text{LW}}B(\text{LST}_{\text{LW}}) + H\cdot\rho_{\text{LW}}C_{32}\cdot\varepsilon_{\text{RW}}B(\text{LST}_{\text{RW}}) + W\cdot\rho_{\text{LW}}(\rho_{\text{RW}}F_{\text{RW}\rightleftharpoons\text{LW}}+1)C_4}{H\cdot m\_\text{denom}} \\ \dfrac{H\cdot(C_{31}-\rho_{\text{LW}}C_3)\cdot\varepsilon_{\text{RW}}B(\text{LST}_{\text{RW}}) + H\cdot\rho_{\text{RW}}C_{32}\cdot\varepsilon_{\text{LW}}B(\text{LST}_{\text{LW}}) + W\cdot\rho_{\text{RW}}(\rho_{\text{LW}}F_{\text{RW}\rightleftharpoons\text{LW}}+1)C_4}{H\cdot m\_\text{denom}} \end{bmatrix} \tag{19}$$

$$C_{11} = 1 - F_{\text{RW}\rightleftharpoons\text{LW}}^2\rho_{\text{LW}}\rho_{\text{RW}} \tag{20}$$

$$C_1 = F_{\text{LW,RW}\to A,\text{Rd}}F_{A,\text{Rd}\to\text{LW,RW}}(2F_{\text{RW}\rightleftharpoons\text{LW}}\rho_{\text{LW}}\rho_{\text{RW}} + \rho_{\text{LW}} + \rho_{\text{RW}}) \tag{21}$$

$$C_{12} = F_{\text{RdA}}C_{11} + C_1 \tag{22}$$

$$C_2 = F_{\text{LW,RW}\to A,\text{Rd}}((F_{\text{RW}\rightleftharpoons\text{LW}}\rho_{\text{RW}}+1)\varepsilon_{\text{LW}}B(\text{LST}_{\text{LW}}) + (F_{\text{RW}\rightleftharpoons\text{LW}}\rho_{\text{LW}}+1)\varepsilon_{\text{RW}}B(\text{LST}_{\text{RW}})) \tag{23}$$

$$\begin{aligned} m\_\text{denom} = {} & \left(F_{\text{Rd}\rightleftharpoons A}^2\rho_A\rho_{\text{Rd}} - 1\right)\left(F_{\text{RW}\rightleftharpoons\text{LW}}^2\rho_{\text{LW}}\rho_{\text{RW}} - 1\right) \\ & -(\rho_{\text{Rd}} + \rho_A(2F_{\text{Rd}\rightleftharpoons A}\rho_{\text{Rd}}+1))(\rho_{\text{RW}} + \rho_{\text{LW}}(2F_{\text{RW}\rightleftharpoons\text{LW}}\rho_{\text{RW}}+1))F_{A,\text{Rd}\to\text{LW,RW}}F_{\text{LW,RW}\to A,\text{Rd}} \end{aligned} \tag{24}$$

$$C_{31} = 1 - F_{\text{Rd}\rightleftharpoons A}^2\rho_A\rho_{\text{Rd}} \tag{25}$$

$$C_3 = F_{\text{LW,RW}\to A,\text{Rd}}F_{A,\text{Rd}\to\text{LW,RW}}(2F_{\text{Rd}\rightleftharpoons A}\rho_A\rho_{\text{Rd}} + \rho_{\text{Rd}} + \rho_A) \tag{26}$$

$$C_{32} = F_{\text{RW}\rightleftharpoons\text{LW}}C_{31} + C_3 \tag{27}$$

$$C_4 = F_{A,\text{Rd}\to\text{LW,RW}}\left((F_{\text{Rd}\rightleftharpoons A}\rho_A + 1)\varepsilon_{\text{Rd}}B(\text{LST}_{\text{Rd}}) + (F_{\text{RdA}}\rho_{\text{Rd}}+1)L^{\downarrow}\right). \tag{28}$$

where L^{Gnd} and T^{Gnd} represent the ground observed radiance and brightness temperature of the target pixel over a street canyon, respectively, with L^{TOA} and T^{TOA} representing the satellite observed radiance and brightness temperature of target pixel over a street canyon, respectively, none of which take into account the impact of 3-D structures and their radiation. In this article, the magnitude of the impact of 3-D structures and their radiation on ground and satellite TIR measurements over a street canyon have been defined as (37) and (38), respectively,

$$\Delta T_{\mathrm{3D\text{-}2D}}^{\mathrm{Gnd}} = T^{\mathrm{Gnd\_3D}} - T^{\mathrm{Gnd}} \tag{37}$$

$$\Delta T_{\mathrm{3D\text{-}2D}}^{\mathrm{TOA}} = T^{\mathrm{TOA\_3D}} - T^{\mathrm{TOA}}. \tag{38}$$

D. Qualification of the Contribution of Atmosphere and Wall-to-Ground TIR Measurements Over a Road

If the target has been observed obliquely, the TIR measurement may be a mixed signal of roof, wall, and road. Under such cases, it is difficult to quantitively investigate the contribution of each radiation source to the total TIR measurements. Therefore, it is assumed that the target is to be observed vertically and the footprint of the IFOV is to be filled only with road in this section, suggesting $\Omega_{\mathrm{roof}}/\Omega_{\mathrm{IFOV}} = \Omega_{\mathrm{wall}}/\Omega_{\mathrm{IFOV}} = 0$ and $\Omega_{\mathrm{road}}/\Omega_{\mathrm{IFOV}} = 1$. Then, (30) could be simplified further as

$$\begin{aligned} L^{\mathrm{Gnd\_3D}} &= \varepsilon_{\mathrm{Rd}} B(\mathrm{LST_{Rd}}) + \frac{\rho_{\mathrm{Rd}} H \cdot F_{\mathrm{LW}\to\mathrm{Rd}} \varepsilon_{\mathrm{wall}} B(\mathrm{LST_{LW}})}{W(1 - F_{\mathrm{RW}\rightleftharpoons\mathrm{LW}}\rho_{\mathrm{wall}})} \\ &\quad + \frac{\rho_{\mathrm{Rd}} H \cdot F_{\mathrm{RW}\to\mathrm{Rd}} \varepsilon_{\mathrm{wall}} B(\mathrm{LST_{RW}})}{W(1 - F_{\mathrm{RW}\rightleftharpoons\mathrm{LW}}\rho_{\mathrm{wall}})} + \frac{\rho_{\mathrm{Rd}} F_{A\to\mathrm{Rd}} L^{\downarrow}}{1 - F_{\mathrm{RW}\rightleftharpoons\mathrm{LW}}\rho_{\mathrm{wall}}}. \end{aligned} \tag{39}$$

Based on (39), the contribution of each radiation source inside the 3-D structures to the total ground TIR measurements over a road can be obtained. The contribution of the atmosphere to the ground TIR measurements ($\Delta T_A^{\mathrm{OnRoad}}$) over a road can be expressed by:

$$\begin{aligned} \Delta T_A^{\mathrm{OnRoad}} &= B^{-1}\left[\varepsilon_{\mathrm{Rd}} B(\mathrm{LST_{Rd}}) + \frac{\rho_{\mathrm{Rd}} F_{A\to\mathrm{Rd}} L^{\downarrow}}{1 - F_{\mathrm{RW}\rightleftharpoons\mathrm{LW}}\rho_{\mathrm{wall}}}\right] \\ &\quad - B^{-1}[\varepsilon_{\mathrm{Rd}} B(\mathrm{LST_{Rd}})] \end{aligned} \tag{40}$$

where B^{-1} is the inverse Planck function.

Similarly, the contribution of the two walls to the ground TIR measurements ($\Delta T_{\mathrm{wall}}^{\mathrm{OnRoad}}$) over a road can be expressed by

$$\begin{aligned} &\Delta T_{\mathrm{wall}}^{\mathrm{OnRoad}} \\ &= B^{-1}[\varepsilon_{\mathrm{Rd}} B(\mathrm{LST_{Rd}}) + \frac{\rho_{\mathrm{Rd}} H \cdot F_{\mathrm{LW}\to\mathrm{Rd}} \varepsilon_{\mathrm{wall}} B(\mathrm{LST_{LW}})}{W(1 - F_{\mathrm{RW}\rightleftharpoons\mathrm{LW}}\rho_{\mathrm{wall}})} \\ &\quad + \frac{\rho_{\mathrm{Rd}} H \cdot F_{\mathrm{RW}\to\mathrm{Rd}} \varepsilon_{\mathrm{wall}} B(\mathrm{LST_{RW}})}{W(1 - F_{\mathrm{RW}\rightleftharpoons\mathrm{LW}}\rho_{\mathrm{wall}})}] - B^{-1}[\varepsilon_{\mathrm{Rd}} B(\mathrm{LST_{Rd}})]. \end{aligned} \tag{41}$$

III. Simulation Results

A. Simulation Inputs

To investigate the impact of 3-D structures and their radiation on the satellite TIR measurements, the geometric and radiative properties of the scenario are needed. From (30)–(33), it is shown that six parameters could affect the magnitude of satellite TIR measurement: atmospheric type, temperature and emissivity of building walls, temperature and emissivity of a road, and the ratio between wall height and road width (hereafter referred as "H/W"). Please note that the temperatures of left and right wall have been set to be the same during the analyses in the following sections for simplification (i.e., $\mathrm{LST_{LW}} = \mathrm{LST_{RW}} = \mathrm{LST_{wall}}$), although they can be different in the proposed ATIMOU. Besides, since the building walls are assumed to have the same height, the energy exchange inside the street canyon will not be affected by the roof-emitted radiance. Therefore, the dependency of the impact

$$\begin{bmatrix} L_{\mathrm{Rd}}^{\mathrm{Gnd\_3D}} \\ L_{A}^{\mathrm{Gnd\_3D}} \\ L_{\mathrm{LW}}^{\mathrm{Gnd\_3D}} \\ L_{\mathrm{RW}}^{\mathrm{Gnd\_3D}} \end{bmatrix} = \begin{bmatrix} \varepsilon_{\mathrm{Rd}} B(\mathrm{LST_{Rd}}) + \frac{\rho_{\mathrm{Rd}} H \cdot F_{\mathrm{LW}\to\mathrm{Rd}} \varepsilon_{\mathrm{wall}} B(\mathrm{LST_{LW}})}{W(1 - F_{\mathrm{RW}\rightleftharpoons\mathrm{LW}}\rho_{\mathrm{wall}})} + \frac{\rho_{\mathrm{Rd}} H \cdot F_{\mathrm{RW}\to\mathrm{Rd}} \varepsilon_{\mathrm{wall}} B(\mathrm{LST_{RW}})}{W(1 - F_{\mathrm{RW}\rightleftharpoons\mathrm{LW}}\rho_{\mathrm{wall}})} + \frac{\rho_{\mathrm{Rd}} F_{A\to\mathrm{Rd}} L^{\downarrow}}{1 - F_{\mathrm{RW}\rightleftharpoons\mathrm{LW}}\rho_{\mathrm{wall}}} \\ L^{\downarrow} + \frac{\rho_A H \cdot F_{\mathrm{LW}\to A} \varepsilon_{\mathrm{wall}} B(\mathrm{LST_{LW}})}{W(1 - F_{\mathrm{RW}\rightleftharpoons\mathrm{LW}}\rho_{\mathrm{wall}})} + \frac{\rho_A H \cdot F_{\mathrm{RW}\to A} \varepsilon_{\mathrm{wall}} B(\mathrm{LST_{RW}})}{W(1 - F_{\mathrm{RW}\rightleftharpoons\mathrm{LW}}\rho_{\mathrm{wall}})} + \frac{\rho_A F_{\mathrm{Rd}\to A} \varepsilon_{\mathrm{Rd}} B(\mathrm{LST_{Rd}})}{1 - F_{\mathrm{RW}\rightleftharpoons\mathrm{LW}}\rho_{\mathrm{wall}}} \\ \varepsilon_{\mathrm{wall}} B(\mathrm{LST_{LW}}) + \frac{\rho_{\mathrm{wall}} W \cdot F_{A\to\mathrm{LW}} L^{\downarrow}}{H(1 - F_{\mathrm{RW}\rightleftharpoons\mathrm{LW}}\rho_{\mathrm{wall}})} + \rho_{\mathrm{wall}} F_{\mathrm{RW}\to\mathrm{LW}} \varepsilon_{\mathrm{wall}} B(\mathrm{LST_{RW}}) + \frac{\rho_{\mathrm{wall}} W \cdot F_{\mathrm{Rd}\to\mathrm{LW}} \varepsilon_{\mathrm{Rd}} B(\mathrm{LST_{Rd}})}{H(1 - F_{\mathrm{RW}\rightleftharpoons\mathrm{LW}}\rho_{\mathrm{wall}})} \\ \varepsilon_{\mathrm{wall}} B(\mathrm{LST_{RW}}) + \frac{\rho_{\mathrm{wall}} W \cdot F_{A\to\mathrm{RW}} L^{\downarrow}}{H(1 - F_{\mathrm{RW}\rightleftharpoons\mathrm{LW}}\rho_{\mathrm{wall}})} + \rho_{\mathrm{wall}} F_{\mathrm{LW}\to\mathrm{RW}} \varepsilon_{\mathrm{wall}} B(\mathrm{LST_{LW}}) + \frac{\rho_{\mathrm{wall}} W \cdot F_{\mathrm{Rd}\to\mathrm{RW}} \varepsilon_{\mathrm{Rd}} B(\mathrm{LST_{Rd}})}{H(1 - F_{\mathrm{RW}\rightleftharpoons\mathrm{LW}}\rho_{\mathrm{wall}})} \end{bmatrix} \tag{29}$$

$$\boldsymbol{M} = \begin{bmatrix} \frac{\Omega_{\mathrm{roof}}}{\Omega_{\mathrm{IFOV}}} & \frac{\Omega_{\mathrm{road}}}{\Omega_{\mathrm{IFOV}}} & \frac{\Omega_{\mathrm{wall}}}{\Omega_{\mathrm{IFOV}}} \end{bmatrix} \tag{32}$$

$$N = \begin{bmatrix} \varepsilon_{\mathrm{roof}} B(\mathrm{LST_{roof}}) + (1 - \varepsilon_{\mathrm{roof}}) L^{\downarrow} \\ \varepsilon_{\mathrm{Rd}} B(\mathrm{LST_{Rd}}) + \frac{\rho_{\mathrm{Rd}} H \cdot F_{\mathrm{LW}\to\mathrm{Rd}} \varepsilon_{\mathrm{wall}} B(\mathrm{LST_{LW}})}{W(1 - F_{\mathrm{RW}\rightleftharpoons\mathrm{LW}}\rho_{\mathrm{wall}})} + \frac{\rho_{\mathrm{Rd}} H \cdot F_{\mathrm{RW}\to\mathrm{Rd}} \varepsilon_{\mathrm{wall}} B(\mathrm{LST_{RW}})}{W(1 - F_{\mathrm{RW}\rightleftharpoons\mathrm{LW}}\rho_{\mathrm{wall}})} + \frac{\rho_{\mathrm{Rd}} F_{A\to\mathrm{Rd}} L^{\downarrow}}{1 - F_{\mathrm{RW}\rightleftharpoons\mathrm{LW}}\rho_{\mathrm{wall}}} \\ \varepsilon_{\mathrm{wall}} B\left(\mathrm{LST_{wall\_}}_x\right) + \frac{\rho_{\mathrm{wall}} W \cdot F_{A\to\mathrm{wall\_}x} L^{\downarrow}}{H(1 - F_{\mathrm{RW}\rightleftharpoons\mathrm{LW}}\rho_{\mathrm{wall}})} + \rho_{\mathrm{wall}} F_{\mathrm{wall\_}y\to\mathrm{wall\_}x} \varepsilon_{\mathrm{wall}} B\left(\mathrm{LST_{wall\_}}_y\right) + \frac{\rho_{\mathrm{wall}} W \cdot F_{\mathrm{Rd}\to\mathrm{wall\_}x} \varepsilon_{\mathrm{Rd}} B(\mathrm{LST_{Rd}})}{H(1 - F_{\mathrm{RW}\rightleftharpoons\mathrm{LW}}\rho_{\mathrm{wall}})} \end{bmatrix}. \tag{33}$$

TABLE I

SIMULATION INPUTS FOR STUDYING THE MAGNITUDE OF THE IMPACT OF 3-D STRUCTURES AND THEIR RADIATION ON TIR MEASUREMENTS

Geometric properties			
H/W	0.5, 1.0, 2.0 (Default), 4.0		
Radiative properties			
	Emissivity (Min, Mean, Max)	Temperature (K)	
Wall	0.415, 0.906 (Default), 0.967	260, 280, 300 (Default). 320, 340	
Road	0.921, 0.950 (Default), 0.973	260, 280, 300 (Default). 320, 340	
Roof	0.016, 0.813 (Default), 0.988	260, 280, 300 (Default). 320, 340	
Atmospheric parameters			
Atmospheric type (Total water vapor content / bottom layer temperature)	Tropical (4.11 g/cm^2 / 300.15 K), Mid-Latitude Summer (2.92 g/cm^2 / 294.15 K), Mid-Latitude Winter (0.85 g/cm^2 / 272.15 K), 1976 US Standard (1.42 g/cm^2 / 288.15 K, Default)		
Viewing angles			
Zenith angle	0° ~ 50°	Azimuth angle	0° ~ 360°

of 3-D structures and their radiation on roof emissivity and temperature will not be discussed in this article. Additionally, simulated results at 10 μm have been presented as an example because the results are similar in other TIR wavelengths. Aerosol type has been set as Urban with the visibility of 10 km and MODerate resolution atmospheric TRANsmission model (MODTRAN) [29], [30] has been introduced to calculate the atmospheric transmittance, upwelling, downwelling radiance, and the atmospheric spherical albedo at bottom of the atmosphere. The IFOV footprint is assumed to be filled only with road at nadir. A series of H/W is set to represent different street canyon structures. Besides, we have obtained the minimum, maximum, and mean emissivities at 10 μm for commonly used construction materials of roof, wall, and road respectively on the basis of the ECOSTRESS emissivity library (https://speclib.jpl.nasa.gov) to represent the emissivity variations in urban areas. When studying the dependency of the magnitude of 3-D structures and their radiation on a specific parameter, the rest arguments have been set as their mean value (tagged as the "default" value in Table I). Detailed configurations for simulation inputs are listed in Table I.

B. Analysis of the Impact of 3-D Structures and Their Radiation on TIR Measurements Over a Street Canyon

According to (31) and (33), atmospheric transmittance, H/W, road reflectance, wall radiation, and viewing direction are the five main factors that exert the strongest influence on the TIR measurements after considering the 3-D structures and their radiation in the radiative transfer model. Therefore, the influence of these first four parameters in function of view geometric conditions on the magnitude of the impact of 3-D structures and their radiation is further investigated using (30)–(38) in this section.

1) Dependency of the Impact of 3-D Structures and Their Radiation on Atmospheric Type: Four atmospheric types were used to represent different atmospheric conditions in this section. Using (38), the magnitude of the impact of 3-D structures and their radiation on satellite TIR measurement was considered for different atmospheric types (Fig. 3). Results are presented utilizing a polar coordinate system with color representing the magnitude of the impact of 3-D structures and their radiation, the length of radius representing the viewing zenith angle, and the radius angle representing the viewing azimuth angle. As the results show, the magnitude of the impact of 3-D structures and their radiation in a hot, humid

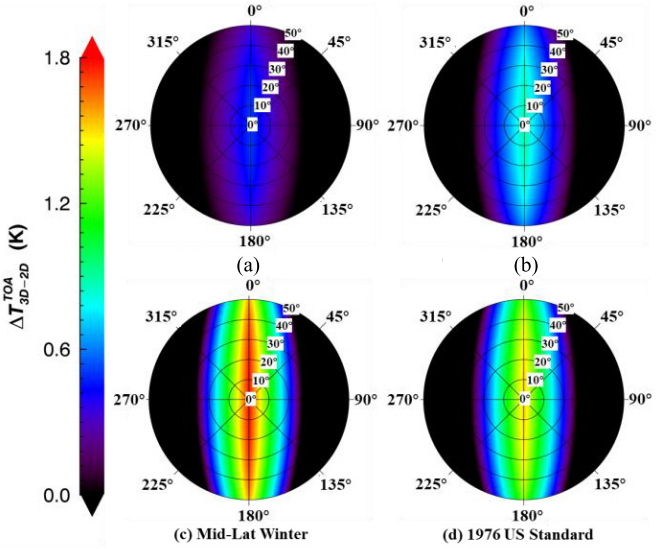

Fig. 3. Magnitude of the impact of 3-D structures and their radiation on satellite TIR measurements over a street canyon for different atmospheric types on the basis of (31), (35), and (38). Additional required parameters have been set as the default values listed in Table I.

atmosphere (e.g., Tropical with total water vapor content of 4.11 g/cm^2 and bottom layer temperature of 300.15 K) is about 0.52 K, which is much smaller than that in a cold and dry atmosphere (e.g., Mid-Latitude Winter with total water vapor content of 0.85 g/cm^2 and bottom layer temperature of 272.15 K) with a magnitude of about 1.78 K. In fact, the difference in the magnitude of the impact of 3-D structures and their radiation for different atmospheres is mainly caused by the variation of atmospheric transmittance. As the atmosphere becomes humid and hot, atmospheric transmittance decreases, indicating that the contribution of 3-D structures and their radiation will be suppressed in the satellite observed signals. This effect explains why the magnitude of the impact of 3-D structures and their radiation in cold and dry atmospheres is always larger than those in hot and humid atmospheres.

Additionally, for each atmospheric type, the impact of 3-D structures and their radiation decreases as viewing zenith angle increases, including the north–south direction. This is believed to be caused by the decrease of atmospheric transmittance with increasing view zenith angle. Moreover, around the west–east direction, IFOV may be partly or entirely filled with building roofs as the viewing zenith angle increases to a certain value. Consequently, with increasing zenith angle, the magnitude of the impact of 3-D structures and their radiation decreases faster toward the west–east direction than those around North–South direction, because the building roofs are not affected by the 3-D structures and their radiation.

2) Dependency of the Impact of 3-D Structures and Their Radiation on Road Emissivity: From (33), it is shown that H/W is a factor that governs the energy exchange inside the street canyon. Besides, road reflectance that directly multiplies the H/W is also an important parameter determining the simulated TIR measurements, especially for nadir observations. Moreover, road reflectance determines not only the amount

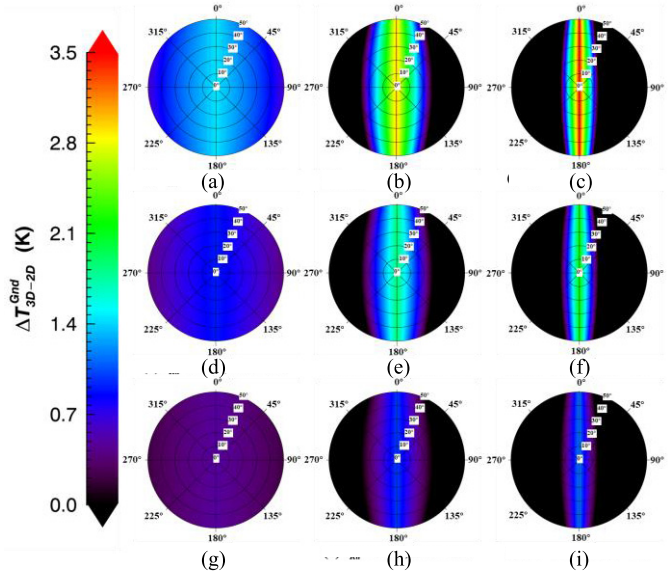

Fig. 4. Magnitude of the impact of 3-D structures and their radiation on ground TIR measurements over a street canyon under different combinations of road emissivity and H/W on the basis of (30), (34), and (37). Additional parameters have been set as the default values listed in Table I.

of reflected environmental radiance, but also the self-emitted radiance of the road ($\varepsilon_{\mathrm{Rd}} = 1 - \rho_{\mathrm{Rd}}$). In this section, (37) is employed under different combinations of road emissivity and H/W to study the impact of 3-D structures and their radiation on ground TIR measurements (Fig. 4).

Results show that the impact of 3-D structures and their radiation increases with increasing H/W around the north–south direction. For example, when road emissivity is 0.921, the magnitude of the impact of 3-D structures and their radiation increases from about 1.44 K to 3.47 K as H/W increases from 0.5 to 4 [Fig. 4(a)–(c)]. However, as H/W increases from 0.5 to 2, the impact of 3-D structures and their radiation increases by about 1.54 K (from 1.44 to 2.98 K). When H/W continually increases from 2 to 4, the impact of 3-D structures and their radiation only increases by about 0.49 K (from 2.98 to 3.47 K), indicating the increasing rate of impact of 3-D structures and their radiation decreases as H/W continually increases. This is because the view factors from wall to road first increase quickly with increasing H/W, then tend to become stable as they approach 0.5, suggesting that the possibility of energy leaving the wall and reaching the road tends to be stable with increasing H/W. Moreover, when H/W is large (e.g., H/W $\geq$ 2), for those cases with a viewing azimuth angle away from the north–south direction and viewing zenith angle larger than 20°, there will be no impact of 3-D structures and their radiation on the TIR measurement because the IFOV is only filled with building roofs. But when H/W is small (e.g., H/W = 0.5), the impact of 3-D structures and their radiation exists for all viewing angles.

Results also show that road emissivity significantly affects the magnitude of the impact of 3-D structures and their radiation. When road emissivity decreases from 0.973 to 0.921, the contribution from 3-D structures and their radiation to the TIR measurements increases by 0.96 K (from 0.48 to 1.44 K) for the cases with H/W = 0.5, while could increase by 2.30 K (from 1.17 to 3.47 K) for the cases with H/W = 4. In fact, as the road emissivity decreases, the target reflected environmental radiance increases, leading to the proportion of the target reflected environmental radiance in the total TIR measurement increases directly. Besides, according to the Kirchoff's law, the road self-emitted radiance decreases at the same time, which could also indirectly result in the increase of the proportion of the target reflected environmental radiance in the total TIR measurement. Therefore, the magnitude of the impact of 3-D structures and their radiation is very sensitive to the road emissivity.

3) Dependency of the Impact of 3-D Structures and Their Radiation on Wall Temperature: For nadir observations, the larger the radiation of the building walls, the larger the impact of 3-D structures and their radiation on the observed TIR measurements, provided that the other parameters remain unchanged. In fact, both wall temperature and wall emissivity determine the radiation emitted by building walls, but the magnitude of the impact of 3-D structures and their radiation is more sensitive to the wall temperature than that to the wall emissivity. As shown in (33), self-radiation of a wall increases with increasing wall emissivity (i.e., the numerator of $\rho_{\mathrm{Rd}} H \cdot F_{\mathrm{LW}\to\mathrm{Rd}} \varepsilon_{\mathrm{wall}} B(\mathrm{LST}_{\mathrm{LW}})/W(1 - F_{\mathrm{RW}\rightleftharpoons\mathrm{LW}}\rho_{\mathrm{wall}}) + ((\rho_{\mathrm{Rd}} H \cdot F_{\mathrm{RW}\to\mathrm{Rd}} \varepsilon_{\mathrm{wall}} B(\mathrm{LST}_{\mathrm{RW}}))/(W(1 - F_{\mathrm{RW}\rightleftharpoons\mathrm{LW}}\rho_{\mathrm{wall}})))$ increases). But the denominator increases as well, which counteracts the increases in the numerator. In addition, the contribution of the atmosphere (i.e., $\rho_{\mathrm{Rd}} F_{A\to\mathrm{Rd}} L^{\downarrow}/1 - F_{\mathrm{RW}\rightleftharpoons\mathrm{LW}}\rho_{\mathrm{wall}}$) also decreases, counteracting the increases in the wall's self-radiation as well. However, as the wall temperature increases, the denominator and the contribution of the atmosphere both remain unchanged which do not counteract the increases of the wall's self-radiation. Consequently, the magnitude of the impact of 3-D structures and their radiation is more dependent on the wall temperature than the wall emissivity, which is also confirmed by the results presented in Section III-C1 below. Therefore, only wall temperature has been changed to represent the differing radiation magnitude of building walls in this section. Using (37), the impact of 3-D structures and their radiation on ground TIR measurement is considered under different combinations of wall temperature and H/W (Fig. 5).

In Fig. 5, it can be seen that the magnitude of the impact of 3-D structures and their radiation on the TIR measurement increases with increasing wall temperature. For cases of nadir observations, as wall temperature increases from 260 to 340 K, the magnitude of the impact of 3-D structures and their radiation increases from about 0.31 K to about 1.75 K if H/W is 0.5. When H/W increases to 4, there will be a more significant impact of 3-D structures and their radiation on the TIR measurement, with the magnitude increasing from 0.77 to 4.21 K. The magnitude of the impact of 3-D structures and their radiation seems to be more affected by wall temperature than by road emissivity when compared with Fig. 4. The possible reason is that the term $\rho_{\mathrm{Rd}} H \cdot F_{\mathrm{LW}\to\mathrm{Rd}} \varepsilon_{\mathrm{wall}} B(\mathrm{LST}_{\mathrm{LW}})/W(1 - F_{\mathrm{RW}\rightleftharpoons\mathrm{LW}}\rho_{\mathrm{wall}}) + ((\rho_{\mathrm{Rd}} H \cdot F_{\mathrm{RW}\to\mathrm{Rd}} \varepsilon_{\mathrm{wall}} B(\mathrm{LST}_{\mathrm{RW}}))/(W(1 - F_{\mathrm{RW}\rightleftharpoons\mathrm{LW}}\rho_{\mathrm{wall}})))$

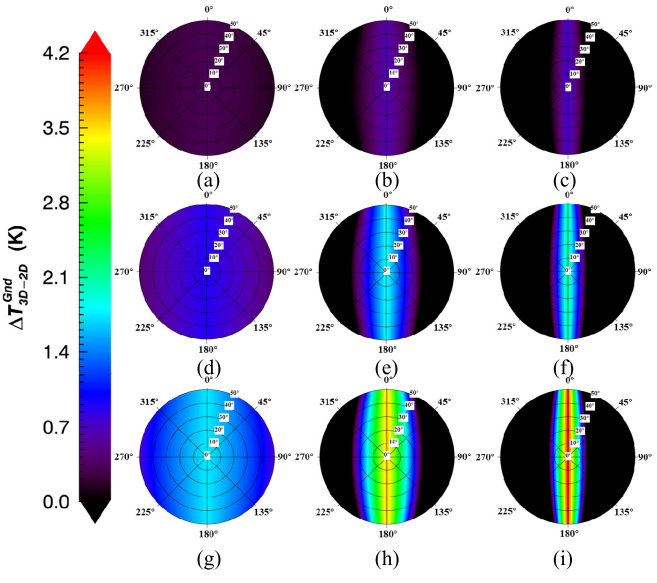

Fig. 5. Magnitude of the impact of 3-D structures and their radiation on ground TIR measurements over a street canyon under different combinations of wall temperature and H/W on the basis of (30), (34), and (37). The temperatures of left and right wall have been set to be the same for simplification (i.e., $\mathrm{LST_{LW}} = \mathrm{LST_{RW}} = \mathrm{LST_{wall}}$). Additional parameters have been set as the default values listed in Table I.

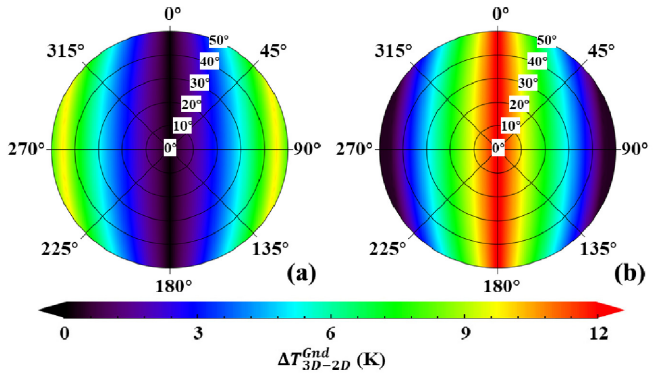

Fig. 6. Magnitude of the impact of 3-D structures and their radiation on ground TIR measurements over a street canyon under two extreme scenarios. The temperatures of left and right wall have been set to be the same for simplification (i.e. $\mathrm{LST_{LW}} = \mathrm{LST_{RW}} = \mathrm{LST_{wall}}$). (a) $\varepsilon_{\mathrm{wall}} = 0.415$, $\mathrm{LST_{wall}} = 300K$, $\varepsilon_{\mathrm{Rd}} = 0.973$, and $\mathrm{LST_{Rd}} = 340K$; (b) $\varepsilon_{\mathrm{wall}} = 0.967$, $\mathrm{LST_{wall}} = 340K$, $\varepsilon_{\mathrm{Rd}} = 0.415$, and $\mathrm{LST_{Rd}} = 300K$. The H/W has been set as 1 and the width of the IFOV has been set as three times as the road width. Additional parameters have been set as the default values listed in Table I.

from (33) is the main influence on the magnitude of the impact of 3-D structures and their radiation. Provided that the other parameters remain unchanged except ρ_{Rd} and $\mathrm{LST_{wall}}$, it is shown that ρ_{Rd} in Fig. 4 has changed from 0.050 to 0.079 and 0.027, respectively, i.e., representing 58% and 46% of the variation in road reflectance, whereas $\mathrm{LST_{wall}}$ has changed from 300 to 340 and 260 K, respectively, i.e., 77% and 53% of the variation exhibited by wall radiance, which is larger than the variation of ρ_{Rd} in Fig. 4. Thus, the magnitude of the impact of 3-D structures and their radiation is smaller with decreasing road emissivity from 0.973 to 0.921 (Fig. 4) than that with increasing wall temperature from 260 to 340 K (Fig. 5).

4) Impact of 3-D Structures and Their Radiation on TIR Measurements for Extreme Cases: According to the simulated results above, there generally exists nonnegligible impact of 3-D structures and their radiation on the ground TIR measurements for typical street canyons. The magnitude of this impact may be even larger for extreme cases, such as the street canyons regarding to a warm road reflected by a low-emissivity wall and a hot wall reflected by a low-emissivity road. In this section, the results of these two scenarios have also been simulated in detail (Fig. 6). It should be noticed that the minimum emissivity of the road has been set as 0.415 in Fig. 6(b) (i.e., the same as the minimum emissivity of the wall), because the typical minimum emissivity of the road according to the ECOSTRESS emissivity library (i.e., 0.921) is too high to represent the extreme condition. The H/W has been set as 1 and the width of the IFOV has been set as three times as the road width to allow a better capture of the signals from walls for oblique viewing angles.

As shown in Fig. 6(a), the magnitude of the impact of 3-D structures and their radiation is only about 0.12 K for nadir observations. This is because the road emissivity is high (0.973), indicating less environmental radiance could be reflected. Moreover, the wall emissivity is low (0.415), leading to less environmental radiance arriving at the road. However, as viewing zenith angle increases, the proportion of the wall inside the IFOV increases. The radiance from a warm road will be reflected by a low-emissivity wall. Therefore, the impact of 3-D structures and their radiation on TIR measurements increases quickly to 9.91 K. As the viewing zenith angle continually increases, the proportion of roof inside the IFOV increases while the proportion of wall decreases. Thus, the impact of 3-D structures and their radiation on TIR measurements decreases as shown in Fig. 6(a).

For the case regarding to a hot wall reflected by a low-emissivity road as shown in Fig. 6(b), the impact of 3-D structures and their radiation is maximum for nadir observations with the magnitude of 12.30 K. As the viewing zenith angle increases, the proportion of road decreases while the proportion of wall and roof increases inside the IFOV. But less environmental radiance could be reflected by the wall because of the high emissivity of the wall and the low emissivity of road, leading to the impact of 3-D structures and their radiation decreases. It is predictable that there will be no impact of 3-D structures and their radiation on the TIR measurements if the viewing zenith angle is large enough to make the IFOV entirely fulfilled by the roof.

C. Analysis of the Contribution of Atmosphere and Wall-to-Total Ground TIR Measurements Over a Road

The separate contribution of atmosphere and wall to the total ground TIR measurements is also worthy of study. Assuming the target has been observed vertically and the IFOV footprint is filled only with road, the contribution of atmosphere and building wall to the total ground TIR measurements over a road can be studied in detail using (40) and (41), respectively.

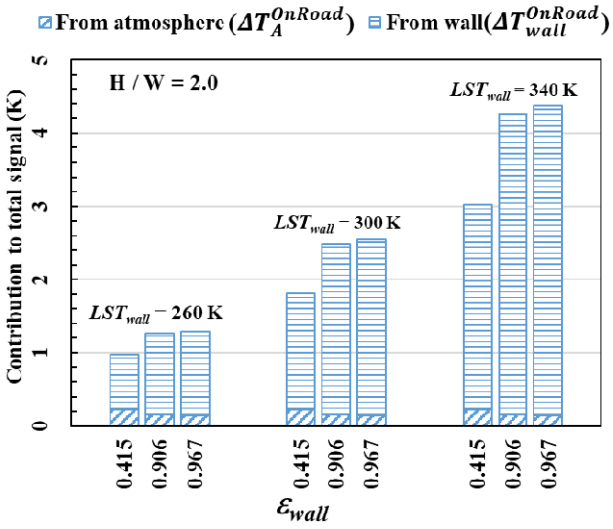

Fig. 7. Respective contributions of atmosphere and building wall to total ground TIR measurements with variation of wall temperature and wall emissivity. The temperatures of left and right wall have been set to be the same for simplification (i.e. LST_{LW}=LST_{RW} = LST_{wall}). Additional parameters have been set as the default values listed in Table I.

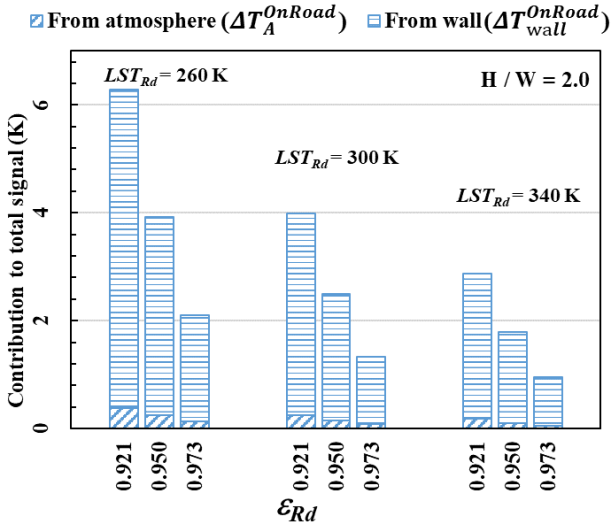

Fig. 8. Respective contributions of atmosphere and building wall to total ground TIR measurements with variation of road temperature and road emissivity. Additional parameters have been set as the default values listed in Table I.

1) Dependency of the Contribution of Atmosphere and Wall-to-Total Ground TIR Measurements With Variable Wall Temperature and Wall Emissivity: When 3-D structures in urban areas are considered, the building walls together with atmospheric downwelling radiance are expected to contribute to the environmental radiance above the road. As the wall temperature and emissivity increase, more energy is emitted from the building walls, provided that the other input parameters remain unchanged (Fig. 7). Consequently, the environmental radiance reflected by a road increases as well. But according to (40), the contribution of atmosphere to the TIR measurements would not change with variation of wall temperature (Fig. 7). In addition, as shown in Fig. 7, the contribution of atmosphere is also not sensitive to the wall emissivity. Furthermore, the magnitude of the contribution of atmosphere to total TIR measurements is small. For example, when H/W is 2, the magnitude is only about 0.22 K for all combinations of wall temperature and emissivity.

Moreover, although the self-emitted radiance of a wall decreases as wall emissivity decreases, more environmental radiance will be reflected by the wall simultaneously. Therefore, the contribution from building walls does not change considerably with a slight variation of wall emissivity (e.g., from 0.967 to 0.906) as shown in Fig. 7. Only if the wall emissivity changes greatly (e.g., from 0.906 to 0.415), the contribution of a building wall would significantly affect the total ground TIR measurements. However, increasing wall temperature could significantly increase the contribution of building walls. For example, as wall temperature rises from 260 to 340 K, the magnitude of the contribution of the building wall could increase from about 1.14 to 4.22 K for cases with H/W of 2 and wall emissivity of 0.967.

2) Dependency of the Contribution of Atmosphere and Wall-to-Total Ground TIR Measurement With Variable Road Temperature and Road Emissivity: The value of road emissivity determines how much environmental radiance could be reflected into the remote sensor. Unlike natural surfaces, the emissivity of manmade materials generally has a large range, implying the reflectivity may be high in urban areas. For example, the emissivity of paving materials such as concrete and asphalt can be <0.95 at 10 μm according to the ECOSTRESS Spectral Library, Version 1.0 (https://speclib.jpl.nasa.gov/). As a result, large environmental radiance could be reflected making the contribution of building wall to total ground TIR measurement significant. As shown in Fig. 8, the contribution of a building wall is <2 K when road emissivity is 0.973, but quickly increases by about 3 times as road emissivity decreases to 0.921.

Moreover, results show that the contribution of a building wall increases with decreasing road temperature. In fact, the absolute value of road-reflected environmental radiance remains the same with varying road temperature, according to (41). However, the self-emitted radiance of a road decreases as road temperature decreases, making the proportion of road-reflected environmental radiance in the total TIR measurements relatively increase. Consequently, the contribution of a building wall and atmosphere to the total TIR measurements both increase with decreasing road temperature. For example, when H/W is 2 and road temperature decreases from 340 to 260 K, the contribution of a building wall increases from 2.71 to 5.89 K for cases with road emissivity of 0.921, whereas the contribution of atmosphere increases from 0.18 to 0.39 K. If road emissivity increases to 0.973, the contribution of a building wall could only increase from 0.90 to 1.97 K and the contribution of the atmosphere is almost negligible at a magnitude of <0.13 K. It is shown that the atmosphere does not make significant contribution to the total TIR measurements for the cases above. But if the road emissivity is low, such as 0.415 (the same as the minimum wall emissivity used in this study), the magnitude of the atmospheric contribution

increases significantly to 2.92 K with the other parameters set as the default values listed in Table I.

IV. Comparison With Other Models

As demonstrated in Section II-B, once the energy exchange inside a street canyon has been calculated, the traditional TIR radiative transfer model could be used to obtain the satellite observed radiance of a target pixel in ATIMOU. Hence, the key procedure of the proposed model is the calculation of ground brightness temperature (T_g). Validation of ATIMOU could be achieved by comparing the simulated T_g with referenced values.

An additional 3-D radiative transfer model has been introduced in this article for intercomparison. Considering that the DART model is one of the most commonly used 3-D radiative transfer models in use and has the ability of simulating radiative transfer in the system "Earth-Atmosphere" from visible to TIR wavelengths [22]–[24], it has been chosen to provide the reference T_g (tagged as DART hereafter). In DART, an Earth scene with the total size of 50 m × 50 m and a cell dimension of 0.5 m × 0.5 m × 0.5 m has been introduced to contain the scenario shown in Fig. 1. The type of roof has been set as a plate without thickness. The surfaces of urban element in DART have been set to have no spatial variability in emissivities and temperatures. The road width, wall height, and other parameters have been set according to the preset values listed in Table I. Then, the scenario of the whole urban area could be generated by repeating this basic Earth scene. Considering the IFOV may be covered with hundreds of cells, the TIR measurements of all the cells inside the IFOV will be averaged to obtain the final simulated results.

In addition, the analytical model proposed by Caselles and Sobrino [25] (tagged as Caselles_1989 hereafter) has also been applied to urban areas to provide the simulated results for intercomparison. Besides, to study the bias introduced by simplifying (19)–(29), the simulated results of ATIMOU using the exact solutions of (19) have also been provided (tagged as ATIMOU_Exact hereafter). Since road emissivity, H/W, wall temperature, and road temperature are the main factors that affect the contribution of 3-D structures and their radiation to total TIR measurements, the simulated T_g using different models has been compared with each other by varying these factors under nadir [Fig. 9(a)–(e)] and nonnadir conditions [Fig. 9(f)]. Besides, since the roof and wall are supposed to be the same component in Caselles_1989, the roof emissivity has been set as the same as the wall emissivity during the comparison of the four models in this section.

For all the cases, it is shown in Fig. 9 that the simulations from ATIMOU_Exact are the closest to DART while the simulations from Caselles_1989 are the most different from DART. The ATIMOU almost provides the same results as the ATIMOU_Exact with the biases of only about 0.05 K. However, as the road emissivity or wall emissivity decreases, the ATIMOU underestimates the T_g comparing with ATIMOU_Exact because of the simplification made in Section II-B, leading to the simulations from ATIMOU less than DART. For example, when all parameters have been set as default values except that road emissivity decreases from 0.973 to 0.921, the difference between ATIMOU and DART

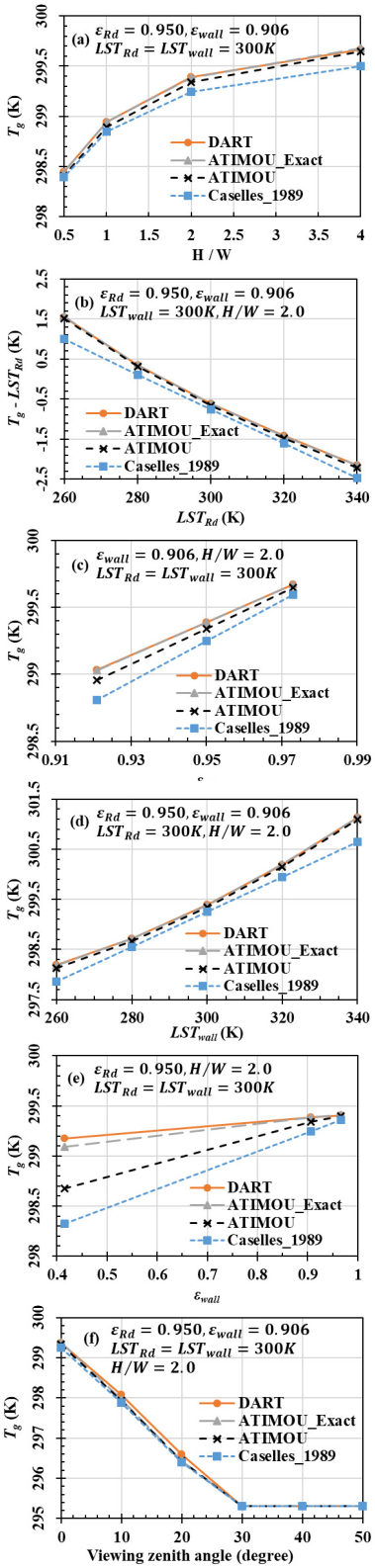

Fig. 9. Intercomparison between the simulated ground brightness temperature (T_g) of the DART, ATIMOU_Exact, ATIMOU, and Caselles_1989 models. The temperatures of left and right wall have been set to be the same for simplification (i.e. $LST_{LW} = LST_{RW} = LST_{wall}$). (a)–(e) IFOV is assumed to only be filled by road, viewing zenith, and azimuth angles are fixed at 0°. (f) Viewing zenith angle varies from 0° to 50° and the azimuth angle is fixed at 90°.

TABLE II
MINIMUM/MEAN/MAXIMUM ABSOLUTE DIFFERENCE OF THE SIMULATED GROUND BRIGHTNESS TEMPERATURE (T_g) BETWEEN ANY TWO OF THE MODELS

	DART	ATIMOU_Exact	ATIMOU	Caselles_1989
DART	-	0.00 K/0.02 K/0.17K	0.00 K/0.10 K/0.50 K	0.02 K/0.32 K/1.93 K
ATIMOU_Exact	-	-	0.01 K/0.09 K/0.42 K	0.02 K/0.31 K/1.87 K
ATIMOU	-	-	-	0.00 K/0.22 K/1.55 K
Caselles_1989	-	-	-	-

increases from 0.02 K to 0.07 K [Fig. 9(c)], which is still acceptable. But if wall emissivity decreases from 0.967 to 0.415 while the other parameters remain as the default values, the difference between ATIMOU and DART increases quickly from 0.01 to 0.50 K [Fig. 9(e)]. As a contrast, the difference between ATIMOU_Exact and DART never exceeds 0.02 K except the one with the wall emissivity of 0.415 [Fig. 9(e)], for which the difference is still not large with the magnitude of 0.08 K.

When comparing ATIMOU with Caselles_1989, the difference is small only if the emissivities of each component inside the street canyon are not too low and the temperatures of each component are close to each other. For example, as shown in Fig. 9(b) the difference between ATIMOU and Caselles_1989 is only around 0.1 K when the road temperature is 300 K and the other parameters have been set as default values. As the road temperature decreases away from 300 to 260 K, the difference between ATIMOU and Caselles_1989 soon increases to 0.53 K. Besides, when the road temperature increases away from 300 to 340 K, this difference also increases to a larger magnitude (0.26 K). When the other parameters have been set as the default values but the wall temperature varies from 300 to 260 or 340 K, the difference between ATIMOU and Caselles_1989 also increases quickly to 0.28 and 0.45 K, respectively [Fig. 9(d)]. This is because Caselles_1989 introduces the first-order Taylor expansion to linearize the Planck function, which maybe not accurate when the temperatures of each component inside the street canyon are not close to the effective temperature. It is also shown that the difference between ATIMOU and Caselles_1989 becomes large when road emissivity or wall emissivity decreases. As shown in Fig. 9(c) and (e), this difference increases from 0.05 to 0.15 K as road emissivity decreases from 0.973 to 0.921, while increases from 0.03 to 0.35 K as wall emissivity decreases from 0.967 to 0.415. This phenomenon is because all the multi-reflections have been ignored in Caselles_1989 but some of the multi-reflections have been retained in ATIMOU owing to the "gain factor - $(1 - F_{\mathrm{RW}\rightleftarrows\mathrm{LW}}\rho_{\mathrm{wall}})$ " in the denominator.

The simulated results of these four models under nonnadir conditions have also been compared as shown in Fig. 9(f). The azimuth angle has been set as 90° which is perpendicular to the street direction and zenith angles of 0°, 10°, 20°, 30°, 40°, and 50° have been used as examples. It is shown that the ATIMOU_Exact is still the closest to DART while the Caselles_1989 is the most different from DART. The simulations from the ATIMOU, ATIMOU_Exact, and Caselles_1989 are generally similar to each other, but the differences between them and DART increase a little as viewing zenith angle increases. This is perhaps because the street canyon has been discretized in DART, indicating there may exist variations among the small voxels that constitute the wall or road after calculating the multi-reflections inside the street canyon. When the viewing zenith angle increases, the scenario inside the IFOV changes resulting from the obstruction of buildings. The simulations of DART vary not only because the proportion of each component inside the IFOV changes, but also because the voxels regarding to each component inside the IFOV are different. However, the surfaces of the wall and road are all considered as Lambert plates in the rest three models, indicating the simulations of these three models vary only because the proportion of each component inside the IFOV changes. Consequently, the difference between DART and the rest three models increases a little with increase of viewing zenith angle. However, if the viewing zenith angle continually increases, only roof could be observed inside the IFOV, leading to the simulated results of the four models are all the same [Fig. 9(f)].

Moreover, to provide an overall comparison between these four models, a series of scenarios have been made to represent different street canyons with varying the H/W, $\varepsilon_{\mathrm{wall}}$, $\mathrm{LST}_{\mathrm{wall}}$, $\varepsilon_{\mathrm{Rd}}$, and $\mathrm{LST}_{\mathrm{Rd}}$ according to the preset parameters in Table I. The other parameters have been set as default values and the viewing direction has been set as nadir. Then, the minimum, mean, and maximum absolute differences between any two of the models have been calculated and listed in Table II on the basis of these scenarios. It is shown that ATIMOU_Exact and DART provide the most similar simulations while Caselles_1989 and DART provide the most different simulations.

V. DISCUSSION AND CONCLUSION

In this article, a new analytical TIR radiative transfer model, ATIMOU, was introduced that considers the impact of 3-D structures and their radiation on TIR measurements. In this model, viewing factors between a road and its surrounding infrastructure were used to calculate the energy exchange inside a street canyon. On the basis of this model, the impact of 3-D structures and their radiation on the TIR measurements over a street canyon was quantitively evaluated under different viewing angles after accounting for obstructions caused by walls of buildings. The respective contributions of the atmosphere and walls to total ground TIR measurements at nadir were also investigated to further characterize the impact of 3-D structures and their radiation. Finally, the fidelity of the proposed model was tested by a comparison with the DART model. Small mean absolute error < 0.10 K was found in the simulated ground brightness temperatures, indicating that the proposed model is in good agreement with DART.

For the simulations over a street canyon, results show that the magnitude of the impact of 3-D structures and their radiation on satellite TIR measurements is different under different atmospheric types. Generally, the magnitude of the impact of 3-D structures and their radiation in a hot, humid atmosphere is smaller than that in a cold, dry atmosphere, and is believed to be caused by the variation of atmospheric transmittance as demonstrated by (31) and (35). Results also

show that the impact of 3-D structures and their radiation is always largest at nadir, because the IFOV may be partly, and even entirely, filled with building roofs as the viewing zenith angle increases. However, the building roofs are not affected by the radiation of the 3-D structures. Moreover, increasing H/W, decreasing road emissivity, and increasing wall temperature could all increase the magnitude of the impact of 3-D structures and their radiation on a TIR measurement, according to the simulations. For nadir observations of a scenario with a wavelength of 10 μm, road and wall temperatures of 300 K, road emissivity of 0.950, and wall emissivity of 0.906, as H/W increases from 0.5 to 4, the impact of 3-D structures and their radiation on the ground TIR measurement increases by about 1.28 K from 0.90 to 2.18 K. If H/W is fixed at 2, while road emissivity decreases from 0.973 to 0.921, the impact of 3-D structures and their radiation could increase from 1 to 2.98 K. If wall temperature increases from 260 to 340 K while the other parameters remain at default values, the impact of 3-D structures and their radiation increases rapidly from 0.66 to 3.62 K. In addition, based on results in Section III-B, the minimum magnitude of the impact of 3-D structures and their radiation on ground TIR measurements is about 0.31 K in cases with road temperature of 300 K, road emissivity of 0.950, H/W of 0.5, wall emissivity of 0.906, and wall temperature of 260 K; whereas a maximum value of about 4.21 K may be obtained in cases with road temperature of 300 K, road emissivity of 0.950, H/W of 4, wall emissivity of 0.906, and wall temperature of 340 K.

The respective contributions of atmosphere and building wall to total ground TIR measurements over a road were also considered. According to the simulations, the contribution of a building wall to the total ground TIR measurements can be greatly affected by radiation from 3-D surroundings. For nadir observations of a scenario with wavelength of 10 μm, the contribution of a building wall is more significant in cases with lower road emissivity and higher wall temperature, because more environmental radiance would be reflected into the remote sensor by the target pixel. For example, if H/W is fixed at 2, road temperature is fixed at 300 K, wall emissivity is fixed at 0.906, and road emissivity is fixed at 0.950, the contribution of a wall increases from 1.12 to 4.12 K with increasing wall temperature from 260 to 340 K. When wall temperature is fixed at 300 K, the contribution of the wall would increase rapidly from 1.69 to 3.69 K as road emissivity decreased from 0.973 to 0.921. Results also show that even though the absolute value of road-reflected environmental radiance remains the same if only the road temperature varies, the contributions of atmosphere and wall to total ground TIR measurement still change. This is because the self-emitted radiance of the road decreases as road temperature decreases, allowing for the proportion of road-reflected environmental radiance in the total TIR measurements to increase. For example, for the cases with H/W of 2, wall temperature of 300 K, wall emissivity of 0.906, and road emissivity of 0.921, the contribution of a wall could increase from 2.71 to 5.89 K as road temperature decreases from 340 to 260 K, whereas the contribution of atmosphere also increases from 0.18 to 0.39 K. In fact, based on the results presented in Section III-C, the radiation from a building wall is the primary cause of the impact of 3-D structures and their radiation on TIR measurement, because the maximum magnitude of the contribution of atmosphere to the total ground TIR measurements is <0.40 K. However, if road emissivity is low, both contributions from the building wall and from the atmosphere cannot be ignored.

To summarize, the impact of 3-D structures and their radiation on the TIR measurements generally cannot be neglected except that the emissivities of the components inside that street canyon are low. Otherwise, the proposed ATIMOU provides a convenient tool to calculate the magnitude of this impact quantitatively and accurately. Since the ATIMOU could provide analytical solutions, it has the potential to be combined with the traditional LST retrieval algorithms to develop new LST retrieval methods with consideration of the urban 3-D structures. Consequently, for high-spatial-resolution TIR images in which the 3-D structures of the street canyon could be recognized, the LST retrieval accuracy should be greatly improved, indicating that the relevant studies which require the urban LST, such as urban heat island and urban energy balance, could all benefit from the more accurate urban LST retrievals.

Nevertheless, this article poses some limitations. The most concerned one is that a symmetric scenario with two equal-height buildings has been used in this article for simplification. However, the two buildings may have different heights in actual canopies. For such cases, there exists energy exchange between the lower building roof and the opposite building wall, leading to the irradiance above the lower building roof dependent on the urban 3-D geometry. Consequently, the current equation system describing the energy conservation inside the street canyon [(7)–(10)] would be affected by the building roof provided that the heights of the two buildings are different. If this asymmetric street canyon has been considered as the combination of one symmetric street canyon similar to Fig. 1 and an extra building on top of one building roof, the energy exchange inside the asymmetric street canyon then could be modeled on basis of article. The derivation will be managed in our future work to improve the proposed ATIMOU.

ACKNOWLEDGMENT

The authors would like to thank Dr. Xiaoyue Gong for her assistance in the English editing.

REFERENCES

[1] M. Anderson, J. Norman, W. Kustas, R. Houborg, P. Starks, and N. Agam, "A thermal-based remote sensing technique for routine mapping of land-surface carbon, water and energy fluxes from field to regional scales," *Remote Sens. Environ.*, vol. 112, no. 12, pp. 4227–4241, Dec. 2008.

[2] R. Zhang, J. Tian, H. Su, X. Sun, S. Chen, and J. Xia, "Two improvements of an operational two-layer model for terrestrial surface heat flux retrieval," *Sensors*, vol. 8, no. 10, pp. 6165–6187, Oct. 2008.

[3] W. Kustas and M. Anderson, "Advances in thermal infrared remote sensing for land surface modeling," *Agricult. Forest Meteorol.*, vol. 149, no. 12, pp. 2071–2081, Dec. 2009.

[4] A. Karnieli *et al.*, "Use of NDVI and land surface temperature for drought assessment: Merits and limitations," *J. Climate*, vol. 23, no. 3, pp. 618–633, Feb. 2010.

[5] Z.-L. Li *et al.*, "Satellite-derived land surface temperature: Current status and perspectives," *Remote Sens. Environ.*, vol. 131, pp. 14–37, Apr. 2013.

[6] F. Sattari and M. Hashim, "A breife review of land surface temperature retrieval methods from thermal satellite sensors," *Middle East J. Sci. Res.*, vol. 22, no. 5, pp. 757–768, Mar. 2014.

[7] J. C. Jiménez-Muñoz and J. A. Sobrino, "A generalized single-channel method for retrieving land surface temperature from remote sensing data," *J. Geophys. Res., Atmos.*, vol. 108, no. D22, pp. 1–9, Nov. 2003.

[8] C. Coll and V. Caselles, "A split-window algorithm for land surface temperature from advanced very high resolution radiometer data: Validation and algorithm comparison," *J. Geophys. Res., Atmos.*, vol. 102, no. D14, pp. 16697–16713, Jul. 1997.

[9] C. Ottlé and D. Vidal-Madjar, "Estimation of land surface temperature with NOAA9 data," *Remote Sens. Environ.*, vol. 40, no. 1, pp. 27–41, Apr. 1992.

[10] Z. Qin, A. Karnieli, and P. Berliner, "A mono-window algorithm for retrieving land surface temperature from Landsat TM data and its application to the Israel-Egypt border region," *Int. J. Remote Sens.*, vol. 22, no. 18, pp. 3719–3746, Jan. 2001.

[11] L. M. Mcmillin, "Estimation of sea surface temperatures from two infrared window measurements with different absorption," *J. Geophys. Res.*, vol. 80, no. 36, pp. 5113–5117, Dec. 1975.

[12] J. A. Sobrino, Z.-L. Li, M. P. Stoll, and F. Becker, "Multi-channel and multi-angle algorithms for estimating sea and land surface temperature with ATSR data," *Int. J. Remote Sens.*, vol. 17, no. 11, pp. 2089–2114, Jul. 1996.

[13] A. Gillespie, S. Rokugawa, T. Matsunaga, J. S. Cothern, S. Hook, and A. B. Kahle, "A temperature and emissivity separation algorithm for Advanced Spaceborne Thermal Emission and Reflection Radiometer (ASTER) images," *IEEE Trans. Geosci. Remote Sens.*, vol. 36, no. 4, pp. 1113–1126, Jul. 1998.

[14] A. Chedin, N. A. Scott, and A. Berroir, "A single-channel, double-viewing angle method for sea surface temperature determination from coincident Meteosat and TIROS-N radiometric measurements," *J. Appl. Meteorol.*, vol. 21, no. 4, pp. 613–618, Apr. 1982.

[15] Z. Wan and Z.-L. Li, "A physics-based algorithm for retrieving land-surface emissivity and temperature from EOS/MODIS data," *IEEE Trans. Geosci. Remote Sens.*, vol. 35, no. 4, pp. 980–996, Jul. 1997.

[16] G. Fontanilles, X. Briottet, S. Fabre, and T. Trémas, "Thermal infrared radiance simulation with aggregation modeling (TITAN): An infrared radiative transfer model for heterogeneous three-dimensional surface-application over urban areas," *Appl. Opt.*, vol. 47, no. 31, p. 5799, Nov. 2008.

[17] S. Pallotta, X. Briottet, C. Miesch, and Y. Kerr, "Sensor radiance physical model for rugged heterogeneous surfaces in the 3-14 μm region.," *Opt. Express*, vol. 14, no. 6, pp. 2130–2150, Mar. 2006.

[18] G. T. Johnson, T. R. Oke, T. J. Lyons, D. G. Steyn, I. D. Watson, and J. A. Voogt, "Simulation of surface urban heat islands under 'IDEAL' conditions at night part 1: Theory and tests against field data," *Boundary-Layer Meteorol.*, vol. 56, no. 3, pp. 275–294, Aug. 1991.

[19] J. A. Voogt, "Thermal remote sensing of urban surface temperatures," Ph.D. dissertation, Dept. Geography, Univ. British Columbia, Vancouver, BC, Canada, 1995.

[20] E. S. Krayenhoff and J. A. Voogt, "A microscale three-dimensional urban energy balance model for studying surface temperatures," *Boundary-Layer Meteorol.*, vol. 123, no. 3, pp. 433–461, May 2007.

[21] V. Masson, "A physically-based scheme for the urban energy budget in atmospheric models," *Boundary-Layer Meteorol.*, vol. 94, no. 3, pp. 357–397, Mar. 2000.

[22] J. P. Gastellu-Etchegorry, E. Martin, and F. Gascon, "DART: A 3D model for simulating satellite images and studying surface radiation budget," *Int. J. Remote Sens.*, vol. 25, no. 1, pp. 73–96, Jan. 2004.

[23] J.-P. Gastellu-Etchegorry *et al.*, "Discrete anisotropic radiative transfer (DART 5) for modeling airborne and satellite spectroradiometer and LIDAR acquisitions of natural and urban landscapes," *Remote Sens.*, vol. 7, no. 2, pp. 1667–1701, Feb. 2015.

[24] P. Guillevic, "Thermal infrared radiative transfer within three-dimensional vegetation covers," *J. Geophys. Res.*, vol. 108, no. D8, pp. 1–13, Apr. 2003.

[25] V. Caselles and J. Sobrino, "Determination of frosts in orange groves from NOAA-9 AVHRR data," *Remote Sens. Environ.*, vol. 29, no. 2, pp. 135–146, Aug. 1989.

[26] F. Becker and Z.-L. Li, "Towards a local split window method over land surfaces," *Int. J. Remote Sens.*, vol. 11, no. 3, pp. 369–393, Mar. 1990.

[27] Z. Wan and J. Dozier, "A generalized split-window algorithm for retrieving land-surface temperature from space," *IEEE Trans. Geosci. Remote.*, vol. 34, no. 4, pp. 892–905, Jul. 1996.

[28] J. R. Howell, R. Siegel, and M. P. Menguc, "Factors from finite areas to finite areas," in *A Catalog of Radiation Heat Transfer Configuration Factors*, 3rd ed. Austin, TX, USA: Taylor, 2010, ch. 1, sec. C, pp. 168–171.

[29] A. Berk *et al.*, "MODTRAN5: A reformulated atmospheric band model with auxiliary species and practical multiple scattering options," *Proc. SPIE, Algorithms Technol. Multispectral, Hyperspectral, Ultraspectral Imag.*, vol. 5571, pp. 78–85, Nov. 2004.

[30] A. Berk *et al.*, "MODTRAN5: 2006 update," *Proc. SPIE, Algorithms Technol. Multispectral, Hyperspectral, Ultraspectral Imag.*, vol. 6233, pp. 1–8, Apr. 2006.

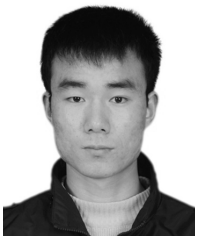

Xiaopo Zheng was born in Nanyang, Henan, China in 1991. He received the B.S. degree in remote sensing science and technology from the China University of Geosciences, Wuhan, China, in 2013, and the M.S. degree in cartography and geographical information system from Peking University, Beijing, China, in 2016. He is pursuing the Ph.D. degree with the University of Strasbourg, Illkirch, France.

Maofang Gao was born in Shandong, China. She received the bachelor's degree in geography from Northeast Normal University, Changchun, China, in 2003, the master's degree in cartography and geography information system from Nanjing University, Nanjing, China, in 2006, and the Ph.D. degree in agricultural remote sensing from the Chinese Academy of Agricultural Sciences, Beijing, China, in 2011.

Since 2006, she has been a Research Staff with the Institute of Agricultural Resources and Regional Planning, Chinese Academy of Agricultural Sciences. She has been an Associate Professor since 2015. Her research interest includes quantitative remote sensing and agricultural drought monitoring.

Zhao-Liang Li received the B.A. degree in photogrammetry from the Wuhan Technical University of Surveying and Mapping, China, in 1985, and the M.S. degree in imaging processing and computer graphics and the Ph.D. degree in terrestrial environmental physics from the University of Louis Pasteur, Strasbourg, France, in 1987 and 1990, respectively.

Since 1992, he has been a Research Scientist with CNRS, Illkirch, France. He joined the Institute of Agricultural Resources and Regional Planning, in 2013. He has participated in many national and international projects such as the National Aeronautics and Space Administration (NASA)-funded Moderate Resolution Imaging Spectroradiometer, European Community (EC)-funded program Exploitation of angular effects in land surface observations from satellites (EAGLE), and ESA-funded programs SPECTRA. He has authored more than 200 articles in international refereed journals. His main expertise fields are in thermal infrared radiometry, parameterization of land surface processes at large scale, and assimilation of satellite data to land surface models.

Kun-Shan Chen (Fellow, IEEE) received the Ph.D. degree in electrical engineering from the University of Texas at Arlington, Arlington, TX, USA, in 1990.

From 1992 to 2014, he was a Professor with National Central University, Taoyuan City, Taiwan. He joined the Institute of Remote Sensing and Digital Earth, Chinese Academy of Science, Beijing, China, in 2014, and the Guilin University of Technology, Guilin, China, in 2019, where his research interests include microwave remote sensing theory, modeling, system, and measurement, and more recently intelligent signal processing and data analytics. He has authored or coauthored over 150 referred journal articles, contributed ten book chapters, coauthored (with A. K. Fung) *Microwave Scattering and Emission Models for Users*, Artech House, 2010, authored *Principles of Synthetic Aperture Radar: A System Simulation Approach*, CRC Press, 2015, and was a Co-Editor (with X. Li, H. Guo, X. Yang) of *Advances in SAR Remote Sensing of Ocean*, CRC Press, FL, USA, 2018.

Dr. Chen serves as a Guest Editor of the special issue of Data Restoration and Denoising of Remote Sensing Data, and special issues of Radar Imaging Theory, Techniques, and Applications, both for *Remote Sensing*, and was a Co-Chair of Technical Committee for IGARSS 2016 and IGARSS 2017. His academic activities include as a Guest Editor of the IEEE TGARS Special Issue on Remote Sensing for Major Disaster Prevention, Monitoring and Assessment in 2007, the Lead Guest Editor of the PROCEEDINGS OF THE IEEE Special Issue on Remote Sensing for Natural Disaster in 2012, the IEEE GRSS Adcom member from 2010 to 2014, a Founding Chair of the GRSS Taipei Chapter, an Associate Editor of the IEEE TRANSACTIONS ON GEOSCIENCE AND REMOTE SENSING since 2000, as a Founding Deputy Editor-in-Chief of the IEEE JOURNAL OF SELECTED TOPICS IN APPLIED EARTH OBSERVATIONS AND REMOTE SENSING from 2008 to 2010. He has served as a member of the editorial board of the PROCEEDINGS OF THE IEEE since 2014.

Xia Zhang was born in Shijiazhuang, Hebei, China in 1985. She received the B.S. degree in geographic information system from Changchun Normal University, Changchun, China, in 2008, and the M.S. and Ph.D. degrees in cartography and geographic information system from Northeast Normal University, Changchun, China, in 2010 and 2014, respectively.

Since 2014, she has been a Lecturer with the College of Land Resources and Urban and Rural Planning, Hebei GEO University, Shijiazhuang, China. Her research interest includes the thermal infrared polarization remote sensing, multiangle and hyperspectral remote sensing and quantitative remote sensing.

Guofei Shang was born in Tangshan, Hebei, China, in 1964. He received the B.E. degree in aerial photogrammetry and remote sensing from Wuhan University, Wuhan, China, in 1985, and the M.E. and Ph.D. degrees in land resources management from the Renmin University of China, Beijing, China, in 1992 and 2002, respectively.

Since 1997, he has been a Professor and the Dean of the College of Land Resources and Urban and Rural Planning, Hebei GEO University, Shijiazhuang, China. His research interest includes the aerial photogrammetry and remote sensing, quantitative remote sensing, and natural resources management.